Cardiolipin clustering promotes mitochondrial membrane dynamics

Kelly E. Zuccaro[a,†], Luciano A. Abriata[b,c,d,†], Fernando Teixeira Pinto Meireles[b,d], Frank R. Moss III[e], Adam Frost[e,f,g,h], Matteo Dal Peraro[b,d,*], and Halil Aydin[a,*]

[a]Department of Biochemistry, University of Colorado Boulder, Boulder, Colorado, USA; [b]Institute of Bioengineering, School of Life Sciences, École Polytechnique Fédérale de Lausanne, CH-1015 Lausanne, Switzerland; [c]Protein Production and Structure Core Facility, School of Life Sciences, École Polytechnique Fédérale de Lausanne, CH-1015 Lausanne, Switzerland; [d]Swiss Institute of Bioinformatics, CH-1015 Lausanne, Switzerland; [e]Department of Biochemistry and Biophysics, University of California, San Francisco, San Francisco, CA, USA; [f]Chan Zuckerberg Biohub, San Francisco, CA, USA; [g]Altos Labs, Bay Area Institute of Science, San Francisco, CA, USA; [h]Quantitative Biosciences Institute, University of California, San Francisco, San Francisco, CA, USA.

[†]These authors contributed equally to this work.

[*]Corresponding author. Email: matteo.dalperaro@epfl.ch; halil.aydin@colorado.edu

Short title: How cardiolipin controls mitochondrial morphology

Keywords: Cardiolipin, phospholipid, OPA1, organelle, mitochondria, membrane dynamics, membrane remodeling, lipid probes, cryoEM

Teaser: This study reveals how CL modulates the activity of OPA1 and how MLCL impacts its ability to govern mitochondrial function.

Abstract

Cardiolipin (CL) is a mitochondria-specific phospholipid that forms heterotypic interactions with membrane-shaping proteins and regulates the dynamic remodeling and function of mitochondria. However, the precise mechanisms through which CL influences mitochondrial morphology are not well understood. In this study, employing molecular dynamics (MD) simulations, we observed CL localize near the membrane-binding sites of the mitochondrial fusion protein Optic Atrophy 1 (OPA1). To validate these findings experimentally, we developed a bromine-labeled CL probe to enhance cryoEM contrast and characterize the structure of OPA1 assemblies bound to the CL-brominated lipid bilayers. Our images provide direct evidence of interactions between CL and two conserved motifs within the paddle domain (PD) of OPA1, which control membrane-shaping mechanisms. We further observed a decrease in membrane remodeling activity for OPA1 in lipid compositions with increasing concentrations of monolyso-cardiolipin (MLCL). Suggesting that the partial replacement of CL by MLCL accumulation, as observed in Barth syndrome-associated mutations of the tafazzin phospholipid transacylase, compromises the stability of protein-membrane interactions. Our analyses provide insights into how biological membranes regulate the mechanisms governing mitochondrial homeostasis.

Introduction

The proper spatial and temporal organization of organelles underlies many cellular processes ranging from division and differentiation to apoptosis and communication (*1*). Within a cell, mitochondria are mainly organized into highly dynamic and interconnected networks, whose diverse functions are dependent on their complex structure and organization (*2*). Mitochondria are double-membrane bound organelles that consist of four major compartments: the outer membrane (OM), intermembrane space (IMS), inner membrane (IM), and matrix (*3*). The mitochondrial IM folds inwards to form the organelle's hallmark cristae membranes, which harbor the respiratory supercomplexes that produce ATP via oxidative phosphorylation (OXPHOS) (*4*). In addition to their role in energy production, mitochondria are involved in the metabolism of amino acids, lipids, and nucleotides, transport of metabolites and ions, reactive oxygen species (ROS) production, and signaling (*4*, *5*). The molecular regulation of mitochondrial architecture, which is controlled by the membrane-shaping lipids and proteins, is critical for tuning the activity of these key processes and preserving homeostasis (*6*–*11*). Hence, mitochondrial function is intimately linked to dynamic changes in mitochondrial morphology and can influence human health and disease (*12*).

The main lipid components of mitochondrial membranes are phospholipids (*13*, *14*). Cardiolipin (CL) is a mitochondrion-specific phospholipid primarily located in the mitochondrial inner membrane (IM), where it accounts for ~20% of the lipid content (*13*, *14*). Characterized by a unique chemical structure consisting of a double glycerophosphate backbone and four fatty acyl chains (*15*), CL undergoes maturation through biosynthesis and remodeling processes catalyzed by different enzymes within mitochondria (*16*–*19*). Mature CL molecules interact with and regulate several pivotal proteins in mitochondria, including those involved in the regulation of mitochondrial morphology (*20*–*26*). Aberrant CL content, structure, and localization result in mitochondrial defects and cellular dysfunction, leading to the development of cardiovascular diseases (*27*), impaired neuronal function (*28*), and neurodegeneration (*29*, *30*). Barth syndrome, an X-linked disease conventionally characterized by dilated cardiomyopathy, skeletal myopathy, cyclic neutropenia, arrhythmias, growth retardation, and cognitive dysfunction, occurs in 1 in 300,000 to 400,000 births (*31*–*33*). The predominant locus for this disorder has been mapped to the distal region of chromosome Xq28, which encodes the human tafazzin (TAZ) (*32*, *34*). TAZ functions as a phospholipid transacylase, facilitating the transfers of acyl groups from phospholipids to monolyso-cardiolipin (MLCL) to generate mature CL species (*16*, *35*). Mutations associated with Barth syndrome compromise TAZ function, resulting in alterations in CL level and molecular composition, along with defects in mitochondrial architecture and function (*36*–*39*). Despite extensive research on the pathophysiology of abnormal CL acyl composition arising from defective remodeling in cellular models, the molecular mechanisms connecting MLCL accumulation and protein function remain poorly understood.

CL plays an essential role in regulating shape and stability of the mitochondrial IM by forming critical interactions with mitochondria-shaping proteins, determining the spatial identity and fitness of the organelle (*21*, *40*, *41*). One such key protein involved in the modulation of mitochondrial architecture is optic atrophy 1 (OPA1), a mechano-chemical enzyme that catalyzes the fusion of mitochondrial IM, reorganizes dynamic cristae structure, and influences OXPHOS efficiency, apoptosis, reactive oxygen species production, and mtDNA maintenance (*42*–*46*). In humans, the OPA1 precursor give rise to eight isoforms, all of which are directed to the mitochondrial intermembrane space (IMS) (*47*). Subsequently, divergent proteolytic mechanisms first cleave the mitochondrial-targeting sequence (MTS) to produce the long form (L-OPA1), which is N-terminally anchored to the inner membrane (IM), followed by the generation of the short form (S-

OPA1) devoid of the transmembrane (TM) domain (*48*, *49*). Both L-OPA1 and S-OPA1, assemble into oligomers and participate in membrane remodeling, and are essential for maintaining mitochondrial organization (*49*). All OPA1 variants and proteoforms assemble into higher-order oligomers in the presence of CL-containing membranes (*10*, *11*, *50–52*). This CL-OPA1 interaction is sufficient to activate membrane fusion and uphold cristae structural integrity, thus highlighting the regulatory role of CL in mitochondrial remodeling and function.

Understanding the precise molecular interactions between key mitochondrial proteins and CL within intact membranes has not been possible because single-phase fluid bilayers are generally thought to lack a structured pattern at the nanoscale. Hence, our understanding of molecular mechanisms connecting CL and mitochondrial protein function remains incomplete. To address this challenge and investigate CL's functional role within the structural organization of mitochondrial membranes, we conducted molecular dynamics (MD) simulations and devised a novel lipid labeling approach for CL localization in electron cryo-microscopy (cryoEM) maps. Our findings reveal how CL regulates the activity of mitochondria shaping proteins to maintain mitochondrial homeostasis and provide a molecular explanation for the mechanisms underlying the disruptive effects of MLCL accumulation on mitochondrial membrane dynamics.

Results

CL molecules cluster near OPA1 membrane binding sites

In a recent study, we reported the cryoEM structures of human S-OPA1 helical assemblies bound to CL-containing lipid tubes (*10*). These findings unveiled the architecture of assembled OPA1 and large structural arrangements potentially involved in catalyzing mitochondrial IM fusion. However, the mechanistic understanding of how OPA1 molecules selectively engage with CL-enriched membranes to modulate mitochondrial morphology remains unclear. To understand the molecular basis of CL-dependent mitochondrial remodeling, we conducted coarse-grained molecular dynamics (CG-MD) simulations on microsecond time scales using S-OPA1 tetramers and lipid bilayers mimicking the composition of the mitochondrial IM (*13*, *14*). While human S-OPA1 forms micron-scale helical filaments upon membrane binding (*10*), simulating filamentous assemblies over relevant timescales proved not feasible due to their large size. Instead, we focused on tetrameric arrangements of S-OPA1 proteins, which encompass all key assembly interfaces, and are tractable through multi-microsecond sampling at the coarse-grained level. To initiate simulations, we extracted four different tetrameric subassemblies (tetramers 1 to 4) of S-OPA1 models representing various oligomeric and functional states of the protein from the cryoEM helical reconstruction of the membrane-bound human S-OPA1 polymer (Fig. 1A, fig. S1A to E). These assemblies were manually positioned with their membrane-interacting surface proximal to, but not fully inserted into, a model membrane composed of a mixture of MARTINI lipids POPC, POPE, and CL at a ratio of ~4:4:2, respectively (fig. S1F). The protein-membrane systems were parameterized with MARTINI22P with close to 1 million beads, representing ~10 million atoms in each system. We simulated each of these 4 tetrameric systems for over 8 μs to assess whether and how the tetramers engage with the lipid membranes. Tetramer 1, representative of the conserved crisscross association of dynamin superfamily proteins (*53*), was simulated in three independent replicas to maximize sampling and allow for the most accurate comparisons (Fig. 1B).

Upon visual inspection, all four subunits of tetramer 1 exhibit clear and strong membrane binding within the first few hundreds of nanoseconds. In this timescale, the highly conserved membrane-inserting loop (MIL) region (residues W771 to R781) of the paddle domain (PD) inserts into the lipid bilayer, firmly anchoring the assembly tightly onto the membrane (Fig. 1B, and figs. S1F and S2). A second highly conserved site within the PD (residues R857 to Y861), which we refer to hereafter as the “docking region”, also interacts with membranes, albeit peripherally. The docking region does not embed in the membrane but remains stably bound throughout the simulation, as quantified below through lipid-protein contact residence times (figs. S1F and S2).

We further observed that concurrently with insertion of the MIL into the membrane, CL rapidly localizes at the protein-membrane contact sites, reaching a higher average density compared to POPC and POPE despite its lower concentration in the lipid membrane (Fig. 1B). While POPC and POPE transiently interact with S-OPA1 membrane contact sites, CL molecules establish much stronger interactions with tetramer 1, demonstrated by residence times 5 to 10 times longer than for the other phospholipids (Fig. 1C). Specifically, analysis of the residence times for contacts between protein residues and cardiolipin molecules revealed extensive engagement of residues within the MIL W771, K772, K773, R774, W775, W778 and R781 as well as residues R857 and R858 residues located in the docking region (Fig. 1C). Mutating these residues of the MIL and docking regions to alanine residues within the same CG MD system abolished the membrane binding activity of the tetrameric subassemblies in simulations and the models remained disengaged in solution while retaining their quaternary structure (fig. S1G).

While the CG simulations already suggest that the positively charged beads of the lysine and arginine residues of the MIL and docking regions engage in contact with the CL's negatively charged beads of CL and tryptophan residues of the MIL interact with the hydrophobic tails of lipids, we examined these interactions in greater detail through all-atom (AA) MD simulations. We first extracted one of the subunits of S-OPA1 tetramer 1 and embedded it in a membrane using the membrane-monomer orientations and interactions retrieved from the CG MD simulations. We ran three replicas of the system for ~1 μs to facilitate free, unbiased exploration of the protein-lipid contacts. Similar to the CG MD simulations, the AA MD simulations revealed clustering of CL around the protein-membrane contact sites in all three replicas. Heavy CL clustering was noticed in particular around the MIL and laterally on R857 and R858 extending towards the docking region (Figs. 1D and E). While the CG MD simulations displayed high density for both the headgroup and acyl chains of CL spanning across the outer leaflet, the AA MD simulations indicate that only the headgroups contributed to the density in the same leaflet. These differences likely arise from the high flexibility of the CL tails, a characteristic only captured in the AA MD simulations.

Despite being only 20% of the membrane composition in all the AA MD simulations, CL accounts for nearly half of the protein-membrane contacts with the membrane-facing residues of the PD (Figs. 1D and E). The key electrostatic interactions are mediated by K772 and R781 of the MIL, R857 and R858 of the docking region, and other critical membrane interface residues within the PD, including K800, R824, K847, and R865. R857 and R858 residues continue to interact completely peripherally with the CL phosphates via their guanidinium groups on the bilayer surface (Figs. 1D and E). This data shows the preference of positively charged residues located at the membrane interface of S-OPA1 for specific interactions with the negatively charged headgroups of CL molecules, thereby recruiting them to the protein-membrane contact sites. However, there is a greater tendency for the CL molecules to be present in the vicinity of the MIL and the docking regions of the PD (Fig. 1E). Analysis of the last 100 ns of each AA MD trajectory reveals an average of ~2 CL molecules in contact with the R857 and R858 residues and ~4 CL molecules around the MIL residues, suggesting that CL molecules are particularly enriched around the MIL region of the PD (Fig. 1E).

The AA MD simulations revealed enriched hydrophobic contacts between CL and S-OPA1 PD near the MIL region. Following the initial protein-membrane contacts, predominantly driven by charge-charge interactions at the solvent-membrane interface, the membrane insertion of the MIL is facilitated by the indole rings of MIL residues W771, W775 and W778. Upon insertion, the tryptophan sidechains become vertically embedded into the spaces in-between lipids, causing the helix comprising the MIL to lodge deep into the membrane by ~10 Å, equivalent to ~25% of the bilayer thickness (Fig. 1E). Mechanistically, the insertion exposes MIL residues to the hydrophobic core of the membrane to facilitate direct interactions with the lipid tails. Interestingly, the three tryptophan residues exhibit less selectivity for the hydrophobic acyl chains of CL upon membrane insertion, forming similar interactions with the acyl chains of POPC and POPE. These findings indicate that charge-charge interactions facilitate the clustering of CL molecules in the vicinity of the PD. Once in close proximity, the CL tails interact with hydrophobic sidechains of the MIL, further stabilizing S-OPA1 subunits on the membrane.

S-OPA1 tetramer is capable of bending membranes

In the presence of CL-containing lipid vesicles, S-OPA1 molecules become activated rapidly and polymerize into membrane-remodeling filaments. This process marks the initial step in reshaping the mitochondrial IM, yet the precise stoichiometry of the OPA1 machinery required for initiating local membrane bending remain unknown. As a member of the dynamin superfamily proteins, OPA1 functions through the oligomerization of its monomeric, dimeric, or tetrameric basic building

blocks into rings or helices to remodel membranes in cells (*53*). Consistent with this notion, our CG MD simulations using S-OPA1 tetramers demonstrate membrane bending in a direction conducive to ring formation of OPA1 proteins on the outer side of the formed tubule (Fig. 1F and fig. S3). Quantitatively, all four tetrameric subassemblies induce positive curvature protruding towards the protein, averaging up to ±0.3 $Å^{-1}$ throughout the simulations at specific points where the membrane contacts the protein (Fig. 1F and fig. S3). For comparison, we measured a control membrane without protein and determined an average fluctuation of ±0.03 $Å^{-1}$ (Fig. 1F). The most curved snapshots of the simulation display local curvature radii ranging from 20 nm to 50 nm, a range consistent with the ~19 nm inner lumen diameter observed in our cryoEM structure of the S-OPA1 polymer wrapped around a membrane tube. A lower curvature radius indicates stronger membrane bending, and the deformations observed in CG MD simulations are likely limited by the strong lateral membrane pressure acting through periodic cells, preventing bending of the lipid bilayer. Similar bending induced by the protein also takes place with the other tetramers, as presented later in the manuscript.

The relative starting poses of S-OPA1 do not affect membrane binding in MD simulations

To address potential biases that may arise due to the initial proximity of S-OPA1 tetramers to the membrane (~6 Å), we conducted a supplementary set of CG MD simulations. In this series, a single subunit of S-OPA1 tetramer 1 was initially positioned 60 Å away from the model membrane (Fig. 1G). Across all five replicas, the S-OPA1 monomer eventually encountered the membrane. Notably, in four of the replicas, extended interactions between S-OPA1 and the bilayer were observed, characterized by the initial charge-charge interactions between the MIL region and the membrane surface, followed by rapid engagement of key tryptophan residues with the membrane and the insertion of the MIL into the bilayer (Fig. 1G). The docking region then formed peripheral interactions with the membrane lipids, positioning the positively charged membrane surface of the PD onto the bilayer. At this stage, the local lipid composition of the membrane patch near the protein contact sites remained unchanged. As the simulations progressed, more contacts were rapidly established between the MIL and docking region residues and membrane lipids, and the number of sidechain-CL interactions increased to ~50% of total contacts in simulations (Fig. 1G). These findings closely mirror our previous observations in CG and AA MD simulations, as well as experimentally determined structural models. Importantly, control CG MD simulations on the membrane without protein did not exhibit aggregation or phase separation of CL molecules, suggesting that S-OPA1 interactions with the lipid bilayer trigger the recruitment of CL molecules to the protein-membrane contact sites. Collectively, our computational findings demonstrate that the main structural element driving OPA1 activation on CL-enriched membranes is the MIL as it facilitates direct binding to CL headgroup and acyl chains. Additionally, the docking region contributes to OPA1-membrane dynamics, albeit to a lesser extent.

The two CL binding motifs contribute to membrane remodeling activity of S-OPA1

To test our computational models of OPA1 in biochemical assays, we employed an *in vitro* reconstitution assay using purified S-OPA1 (fig. S4) and liposomes prepared with various lipid compositions (table S2A). We reconstituted human S-OPA1 WT samples onto lipid bilayers and quantified the membrane binding and remodeling activity of the protein by using co-sedimentation assays and negative-stain transmission electron microscopy (TEM) (figs. S4C and D). Consistent with our previous findings, analysis of the reconstitution assays revealed that S-OPA1 molecules fail to bind and remodel lipid vesicles when CL is omitted from lipid compositions (figs. S4C and D). This confirms that CL enhances the membrane binding and remodeling activity of S-OPA1. To verify the functional relevance of two CL binding motifs, we created, recombinantly expressed, and purified three mutant constructs, as well as the WT construct. Two alanine point mutations were separately introduced in the positively charged docking region motif, R857A and R858A.

The third mutant focused on a charged and hydrophobic motif (^{771}WKKRWxxWKxR^{781}) in the MIL region and converted it to a polyalanine stretch. The co-sedimentation assays determined ~14 and ~8% reductions in membrane binding activity with the R857A and R858A mutations, respectively, while the MIL mutant caused a ~23% decrease in binding compared to the WT. Therefore, all three mutants exhibit decreased membrane binding activity on CL-enriched liposomes (Figs. 2A and B). We then determined that R857A, R858A, and MIL polyalanine mutations impair S-OPA1's ability to form ordered assemblies and remodel CL-containing lipid membranes *in vitro* (Fig. 2C). Our biochemical data indicates that the two conserved motifs form stable interactions with CL molecules, ensuring the proper assembly of OPA1 polymers on the membrane and promoting mitochondrial morphology remodeling.

Structure of S-OPA1 assembly bound to membranes containing contrast-enhancing probes

To experimentally determine CL localization near OPA1 contact sites, we synthesized CL with bromine atoms added to the unsaturated fatty acyl chains. This modification capitalizes on the lipophilicity, steric, and enhanced electron scattering properties of Br that results in dibrominated lipid tails mimicking unsaturated tails, facilitating the determination of the position of CL molecules within the structural organization of intact lipid bilayers (Fig. 3A and fig. S5) (*54*, *55*). We reconstituted human S-OPA1 onto lipid bilayers (both vesicles and nanotubes) containing brominated CL and learned that S-OPA1 can self-organize into higher-order structures on these bilayers and induce the protrusions of narrow lipid tubes (fig. S5E). This observation indicates that the brominated CL, which yields stronger electron scattering, exhibits similar membrane packing properties, and behaves indistinguishably from unsaturated phospholipids *in vitro*. To measure and model the interactions between CL and OPA1, we prepared samples for cryoEM and recorded images of S-OPA1 filament segments bound to brominated CL-containing lipid tubes using a 300-kV Krios cryoEM microscope (fig. S6 and table S1). Image segments were first aligned and averaged to obtain *ab initio* 3D reconstructions, followed by 3D classification to generate well-ordered subsets using the Relion software (figs. S6 and S7) (*56*). However, the membrane-bound assemblies exhibited slightly variable tubule diameters, hindering coherent inter-tube averaging and resulting in multiple conformational classes. To address this variability, we performed 3D classification without alignment and identified filament segments with nearly uniform diameters. The best quality maps were then refined to obtain a sub-nanometer reconstruction of S-OPA1 polymer bound to brominated lipid membranes (fig. S7). The density map distinctly delineates two components corresponding to the protein coat and lipid bilayer, with numerous S-OPA1 subunits forming a spiraling homomeric filament on membranes (Fig. 3 and fig. S6). This reconstruction represents the membrane-proximal conformation of the OPA1 assembly, wherein the PD is docked on the membrane surface and the MIL is embedded in the lipid bilayer (Figs. 3B, C, and D).

The final 3D reconstruction of the membrane-bound S-OPA1 polymer reveals an outer diameter of 48.4 nm and an inner lumen diameter of 19.1 nm (Fig. 3D). It exhibits a three-start helical structure with a rise of 7.69 Å and a twist of 128.642 degrees, with minimal intersubunit connectivity arising from the low packing density of the S-OPA1 lattice (Figs. 3B and C, figs. S6 and S7, and table S1). The cryoEM density map achieved sufficient resolution to unambiguously assign the orientation of the S-OPA1 domains. While the bundle-signaling element (BSE), stalk, and PD could be resolved, the distal GTPase domains that are not interacting with the lipid bilayer were at the lower local resolution, indicating the dynamic nature and conformational flexibility in the membrane-bound state (fig. S6D). Nonetheless, leveraging this reconstruction and prior structural knowledge enabled us to build precise molecular models of S-OPA1 tetramers bound to brominated lipid membranes with an overall resolution of 6.4 Å (Fig. 3 and figs. S6 and S7). A

comparison of membrane-bound OPA1 models from native and brominated liposomes showed highly similar structures with a root-mean-square deviation (RMSD) of only 0.78 Å over 698 Cα atoms of the protein (fig. S6E). These findings collectively indicate that bromine labeling of CL acyl chains does not induce notable structural changes in how OPA1 assembles on lipid membranes.

CryoEM structure confirms CL accumulation at protein contact sites

To detect the position of CL molecules in the reconstructions, we investigated the membrane layer of the experimental density map for focal enrichment of CL-Br. Initially, we normalized the pixel value distributions to the S-OPA1 intensity from radial averages and obtained horizontal and vertical slices of brominated and non-brominated reconstructions (Fig. 3D and fig. S8). The density map confirmed that the docking and the MIL regions of the PD are positioned to make direct interactions with CL molecules in the lipid bilayer (Fig. 3D and fig. S8). Comparing the Coulombic potentials from the resulting 3D maps of unlabeled versus labeled membrane tubes, we located the surplus signals attributable to halogen scattering near OPA1 contact sites in the outer leaflet (Fig. 3D and fig. S8). Further investigation of the outer leaflet between unlabeled and labeled membranes revealed that the delta intensity of our maps indicates local enrichment of CL-Br to the MIL region, with lower delta intensity signals of CL-Br to the left of the MIL suggesting direct interaction with the MIL region (fig. S8). Although CL clustering near OPA1 contact sites was observed, the bilayers remained compositionally heterogeneous with CL-Br distributed throughout the bilayers as observed in the difference map between the CL membrane and CL-Br membrane (Fig. 3E and fig. S8E). In CG MD simulations, CL molecules form frequent but short-lived interactions with the membrane-facing residues of OPA1 PD. Thus, the combined experimental and computational data imply the dynamic nature of CL within lipid bilayers. These results collectively demonstrate that halogenated lipids scatter electrons strongly, enabling the quantitative localization of surplus scattering in our cryoEM maps to estimate the changes in CL concentration within each leaflet. Additionally, identifying preferential sites for OPA1-CL interactions within the membrane-bound S-OPA1 polymer map and matching these sites to those identified by MD simulations provided us a platform to infer structural details at higher resolution.

S-OPA1 interactions with MLCL-containing membranes in simulations

Next, we investigated whether the accumulation of MLCL in lipid bilayers affects OPA1's ability to reshape membranes and control the dynamic architecture of mitochondria. To determine the molecular basis of MLCL-OPA1 interactions, we utilized CG-MD simulations with the same four tetramers of S-OPA1. We assessed how the replacement of CL by MLCL affects OPA1's interactions with membranes. All parameters and the overall setup remained identical to the previous CG-MD simulations, except for the substitution of CL with MLCL. After >8μs of CG-MD simulations, all replicas of the trajectories for the four models revealed membrane binding and clustering of MLCL around the same CL binding motifs. Additionally, they exhibited similar protein-lipid interaction profiles and residence times compared to CL contacts.

To quantitatively analyze the MLCL-protein interactions, we measured the residence times of MLCL in the presence of S-OPA1 tetramers and compared them to the CL residence times. Within the uncertainty of the sampling in the CG MD simulations, residence times for protein-lipid contacts were similar between MLCL and CL (fig. S9A). Similarly, MLCL- and CL-containing lipid bilayers displayed a similar number of protein-lipid contacts per residue in AA MD simulations, despite MLCL containing one fewer acyl chain (fig. S9B). Collectively, our MD simulations at CG and AA resolutions revealed no major differences in how human OPA1 interacts with membranes containing CL or MLCL.

MLCL accumulation impairs OPA1's ability to bend and remodel membranes

Despite the similar protein-lipid interactions and residence times observed with MLCL and CL in the bilayers, the deformation experienced by the MLCL-containing membranes is substantially weaker, especially with assemblies mediated by the conserved crisscross association of S-OPA1 monomers (tetramers 1 and 3) (Fig. 4A and fig. S3). The simulation results suggest the differences in the spontaneous curvature and other material properties of CL and MLCL are critical for OPA1-mediated membrane remodeling with CL enabling membrane shape plasticity and bilayer deformation upon protein binding. To experimentally probe the mechanistic basis of MLCL interactions with human OPA1, we performed co-sedimentation experiments with S-OPA1 and liposomes containing increasing concentrations of MLCL in place of CL (table S2). We found the presence of 1% to 15% of MLCL in liposomes decreases the membrane binding activity of S-OPA1 by ~10% compared to liposomes containing 25% CL (Figs. 4B and C). Increasing concentrations of MLCL up to 25% further diminished S-OPA1's ability to bind liposomes, resulting in a ~20% decrease in membrane binding (Figs. 4B and C). These findings indicate that MLCL forms less stable interactions with OPA1 molecules, resulting in the diminished ability for OPA1 to bind liposomes. While we were able to detect reduced membrane binding activity in these assays, the presence of MLCL did not abolish S-OPA1's ability to bind membranes, consistent with MD simulations.

Following this, we investigated the impact of MLCL on the membrane remodeling activity of S-OPA1. We reconstituted S-OPA1 WT with CL- and MLCL-containing liposomes and monitored the protein's oligomerization and membrane remodeling activity using negative-stain TEM imaging (fig. S10). While the reconstitution of S-OPA1 on CL-containing liposomes resulted in the formation of higher-order protein assemblies and further tubulation of membranes, the replacement of CL by MLCL impaired the oligomerization and liposome remodeling activity of the protein and resulted in protein aggregates around lipid vesicles (Fig. 4D). Even when the MLCL concentration was lowered to 1% in the lipid composition, the activity of the protein was not recovered. This suggests that even the lower molar concentrations of MLCL in lipid bilayers are enough to interrupt OPA1 polymerization on membranes, which is detrimental to OPA1-mediated mitochondrial remodeling (Fig. 4D). Overall, while we only observed modest differences in how OPA1 binds CL- and MLCL-containing lipid bilayers in both MD simulations and co-sedimentation experiments, our membrane remodeling experiments demonstrate that MLCL dampens OPA1's ability to form stable oligomers for membrane remodeling. We propose that MLCL accumulation leads to less favorable protein-membrane interactions, thereby preventing the formation of the helical protein coat required for membrane tubulation.

In our proposed mechanism, OPA1 proteins are recruited to the membrane via specific interactions with CL molecules, which are randomly distributed throughout the membrane with potential pre-formed patches enriched in CL within the lipid bilayer. Upon protein binding, CL molecules rapidly localize to the outer leaflet of the bilayer near the protein-membrane contact sites, facilitating the formation of stable interactions between OPA1 and lipid bilayers. By leveraging these specific CL contacts, OPA1 proteins then assemble into higher-order assemblies required for membrane bending and fusion of the mitochondrial IM. The partial replacement of CL by MLCL, even at low concentrations, destabilizes OPA1 polymerization, thereby hindering membrane remodeling by human OPA1 (Fig. 5).

Discussion

To delve into the intricate dynamic consequences governed by lipid-lipid and lipid-protein interactions in complex and crowded cellular membranes, we performed CG and AA MD simulations. These simulations were set up with various OPA1 structures and the membrane bilayer mimicking the lipid composition of the mitochondrial IM. Dynamic models generated through these simulations revealed the CL clustering within the bilayer, exhibiting leaflet localization and close proximity to the OPA1 contact sites. Furthermore, our computational approach enabled us to accurately measure the lateral chemical organization and morphological changes in CL-enriched membranes that often occur at shorter time and length scales and are challenging to probe experimentally at the molecular level. These analyses led to the identification of two highly conserved binding motifs located at the MIL and docking regions of the PD, showcasing strong interactions with CL molecules within intact lipid membranes (fig. S2). The CL binding motifs establish critical hydrogen bonds and hydrophobic interactions with both the headgroup and acyl chains of CL, reminiscent of protein complexes observed in oxidative phosphorylation (*23*, *24*) and thereby facilitate membrane remodeling. As anticipated, mutations of the key residues to alanine hindered the membrane binding and remodeling activity of OPA1 in our computational and biochemical assays. Note that our reconstitution assays and MD simulations offer an approximation of biological membranes. Our results align with previous studies, demonstrating that mutations to membrane-interacting residues of OPA1 result in fragmented mitochondrial morphology in living cells (*10*, *11*). Overall, these studies allowed us to pinpoint specific lipid-protein interactions and understand how CL regulates the activity of OPA1 to maintain mitochondrial homeostasis.

Determining the functional role of CL within the structural framework of intact lipid bilayers poses challenges due to the heterogeneity and dynamic nature of mitochondrial membranes. Prior research has demonstrated that brominated and iodinated lipids behave similarly to their native counterparts and can serve as contrast-enhancing probes to delineate specific lipids within membranes (*54*, *55*). Moreover, the utilization of bromo-substituents on aliphatic double bounds has a well-established history as fluorescence quenchers in model membranes (*57*–*59*). By labeling CL with halogen atoms, which scatter electrons more strongly than acyl chains alone, we quantitatively located the surplus scattering in our cryoEM maps and estimated the concentration of CL within each leaflet. Our observations of the OPA1 structure bound to brominated membranes provide experimental evidence that specific interactions between CL and OPA1 promote the remodeling of mitochondrial membranes. We anticipate that this versatile tool will prove instrumental in determining how CL either activates or inhibits other key membrane-associated processes in the regulation of mitochondrial morphology and function.

Barth syndrome (BTHS) stands as a significant X-linked cardiomyopathic disease characterized by perturbations of cardiolipin (CL) metabolism in mitochondria (*31*, *32*). Despite its prevalence, the precise repercussions of altered lipid content underlying BTHS symptoms remains unclear. Here, we sought to determine how loss of CL content and accumulation of MLCL in mitochondrial membranes influence the activity of the key membrane remodeling enzyme, OPA1. OPA1 governs mitochondrial shape, cristae integrity, and functional output for a vast array of essential metabolic pathways and processes that determine cell function and fate. Initially, we investigated the impact of MLCL accumulation on OPA1-membrane interactions via MD simulations and measured the dynamics of the lipids throughout the bilayer to determine whether MLCL molecules were also enriched at the protein-membrane contact sites in the bilayer. Our simulations with CL-enriched membranes demonstrated that even though the CL molecules continuously diffuse throughout the membrane, they frequently associate with the two CL binding motif residues. For

instance, the interactions between the key binding motif residues W775, R857, and R858 and CL persisted for 1 μs to 1.5 μs in residence times, which correspond to ~18% of the total simulation time. On the other hand, we also observed similar S-OPA1-membrane contacts when CL was replaced with MLCL in lipid compositions and measured comparable MLCL residence times for most of the MIL and docking region binding motif residues. This outcome is unsurprising, given that the main components mediating the initial protein-membrane interactions are the membrane facing lysine and arginine residues of the PD and negatively charged headgroups of CL and MLCL. The initial steps are followed by the MIL insertion in the membrane, and the subsequent association with the hydrophobic acyl chains of phospholipids sharing similar physicochemical properties. However, the presence of MLCL hindered OPA1's ability to bend membranes in MD simulations. Further probing of mechanistic links between MLCL and OPA1 activity through biochemical assays unveiled that the replacement of CL with MLCL impairs OPA1's ability to form helical assemblies and remodel membranes. In these assays, S-OPA1 was able to bind but not remodel the membranes that contained increasing MLCL concentrations. Interestingly, even partial replacement of CL with low molar concentrations of MLCL in membranes also impaired OPA1-mediated membrane remodeling. Together, these findings indicate that OPA1-MLCL interactions impact OPA1's ability to complete the intermediate helical assembly steps in the pathway to membrane tubulation and fusion.

Understanding MLCL interactions with mitochondrial proteins is critical for determining the molecular basis of pathologies associated with MLCL accumulation (*60*). A distinctive feature of MLCL is the absence of an acyl chain, which may reduce the spontaneous curvature of CL (*61*, *62*). This absence may increase the rigidity of the membrane, making it less susceptible to bending. The differences in the chemical structure could influence the conformation of acyl tails and the accessibility of the headgroup due to hydrogen bonding with the additional hydroxyl group in MLCL, thereby affecting lipid conformations in the vicinity of MLCL. In the context of human OPA1, alterations in membrane lipid composition disrupt key interactions on membranes, preventing the formation of ordered OPA1 assemblies required for membrane remodeling. Additionally, membrane binding and remodeling are interconnected processes occurring at different regulatory steps that modulate OPA1 activity. It is plausible that moderate differences in membrane binding could have drastic effects on the more energy-demanding membrane remodeling steps. Overall, these findings indicate that MLCL-containing membranes exhibit greater resistance to protein-mediated shape changes and provide insights into the disruptive effects of MLCL accumulation on mitochondrial membrane dynamics.

CL is a pivotal regulatory lipid playing critical roles in various mitochondrial processes, including energy production, apoptosis, mitophagy, oxidative stress, and mitochondrial fusion and fission, which govern mitochondrial shape and function. Yet, for many of these cellular processes, it is currently unknown how the role of CL extends from maintaining membrane structure to an intimate association with mitochondrial proteins and how MLCL build-up in membranes impacts their function. Central to these processes is the intricate interplay between CL and the OPA1 protein that results in the initiation of OPA1-mediated mitochondrial membrane remodeling and maintenance of a healthy organellar network distributed throughout the cell. Thus, CL assumes a direct and regulatory role in structural and functional remodeling of mitochondria. Despite the longstanding recognition of the significance of CL in modulating mitochondrial morphology and function, the precise mechanisms through which CL regulates these essential cellular machines, as well as the impact of the MLCL accumulation on mitochondrial membrane remodeling, remains unclear. Our findings highlight how CL molecules cluster near the membrane-binding surfaces of OPA1's PD, engaging in charged and hydrophobic interactions with the conserved PD residues to modulate the activity of the membrane-remodeling enzyme. Moreover, we describe how MLCL

build-up in lipid membranes disrupts OPA1's ability to remodel membranes, potentially playing an important role in the pathogenesis of inherited disorders, such as Barth Syndrome. These insights provide a critical structure-function foundation for understanding the mechanisms connecting CL and regulation of mitochondrial morphology, thus establishing a molecular basis for shaping the mitochondrial IM in health and disease.

Materials and Methods

Cloning, expression and purification.

The gene fragment corresponding to S-OPA1 (Addgene plasmid ID: 26047; residues 252-960) was subcloned into the pCA528 vector, incorporating an N-terminal 10X His tag followed by a SUMO solubility tag. S-OPA1 mutations were engineered using a modified QuickChange Mutagenesis protocol and confirmed through Sanger Sequencing. All S-OPA1 variant constructs were transformed into BL21 DE3-RIPL competent cells. A single colony from each transformation was inoculated into lysogeny broth (LB) media (100 ml) and was grown overnight at 37 °C with kanamycin (50 $\mu g\ mL^{-1}$) and chloramphenicol (25 $\mu g\ mL^{-1}$). The overnight culture (10 ml) was used to inoculate a 750 ml culture of ZYP-5052 auto-induction media and was grown at 37 °C until the optical density at 600 nm (OD_{600}) reached a value between 0.6 and 0.8. At this point, the temperature was reduced to 18 °C within the shaker, and cultures continued to grow overnight for an additional 16 hours. Following the 16-hour induction period, the cells were harvested via centrifugation and stored at -80 °C.

The frozen bacterial pellets were thawed, resuspended with lysis buffer (50 mM HEPES-NaOH, pH 7.5, 500 mM NaCl, 20 mM imidazole, 5 mM $MgCl_2$, 5 mM CHAPS (Anatrace), 5 mM 2-mercaptoethanol, 10% (v/v) glycerol) supplemented with 0.5% Triton X-100, 0.5 mg DNAseI, 1X EDTA-free complete protease inhibitor cocktail (Roche), and lysozyme. The cells were then lysed using an Emulsiflex C3 homogenizer. To remove the cell debris, the lysate was centrifuged at 35,000 x g for 45 minutes at 4 °C. Meanwhile, a Ni-NTA (Qiagen) affinity column was equilibrated with lysis buffer. The supernatant was then filtered through a 0.45 μm membrane (Millipore), and transferred to a column, where it was incubated with the Ni-NTA beads on a roller for 1 hour at 4 °C. The column was then washed with 10 column volumes (CV) of lysis buffer followed by 10 CVs of high salt buffer (50 mM HEPES-NaOH, pH 7.5, 1 M NaCl, 20 mM imidazole, 5 mM $MgCl_2$, 5 mM CHAPS, 5 mM 2-mercaptoethanol, and 10% (v/v) glycerol) and high imidazole buffer (50 mM HEPES-NaOH, pH 7.5, 500 mM NaCl, 80 mM imidazole, 5 mM $MgCl_2$, 5 mM CHAPS, 5 mM 2-mercaptoethanol, and 10% (v/v) glycerol) washes. The sample was then eluted with 10 CVs of elution buffer (50 mM HEPES-NaOH, pH 7.5, 500 mM NaCl, 500 mM imidazole, 5 mM $MgCl_2$, 5 mM CHAPS, 5 mM 2-mercaptoethanol, and 10% (v/v) glycerol). Following elution, the N-terminal 10XHis-SUMO tag was cleaved using Ulp1 enzyme while dialyzing against the FPLC buffer (50 mM HEPES-NaOH, pH 7.5, 500 mM NaCl, 5 mM $MgCl_2$, 5 mM CHAPS (Anatrace), 5 mM 2-mercaptoethanol, 10% (v/v) glycerol) at 4 °C. The digested protein samples were then concentrated with an Amicon Ultra (Millipore) concentrator (50 kDa MWCO) and subjected to further purification using a Superdex-200 16/60 column (Cytiva) equilibrated with the FPLC buffer for further purification. Pure fractions were pooled, concentrated to 2 mg mL^{-1}, aliquoted, flash-frozen with liquid nitrogen, and stored at -80 °C for further use.

Preparation of lipid vesicles and nanotubes.

All lipids, except for brominated cardiolipin (CL-Br), were purchased from Avanti Polar Lipids. Stock solutions were prepared by dissolving lipids in a chloroform, methanol, and water mixture (20:9:1, (v/v/v)) and stored in glass vials at -20 °C. The lipids in this study, 1-palmitoyl-2-oleoyl-glycero-3-phosphocholine (POPC), 1-palmitoyl-2-oleoyl-sn-glycero-3-phosphoethanolamine (POPE), L-α-lysophosphatidylinositol (Soy Lyso PI), cardiolipin (1',3'-bis[1,2-dioleoyl-sn-glycero-3-phospho]-glycerol (CL $(18:1)_4$), and monolyso-cardiolipin (MLCL (94.6% 18:2 and 2.6% 18:1)) were used as purchased without any modification. CL-Br was prepared by adapting previously described procedures for brominating alkenes in the lipids (*54*, *57*). Briefly, CL was dissolved in 5 mL of chloroform (ACS grade) and placed in a scintillation vial on ice. Liquid bromine,

stoichiometric to the number of double bonds (Sigma Aldrich), was slowly added dropwise while the lipid solution was stirred on ice. The vial was then sealed and stirred on ice for 30 minutes in the dark. Solvent and excess bromine were removed under vacuum overnight, and the product was stored under a nitrogen atmosphere at -80 °C. The presence of bromine atoms on CL was confirmed with mass spectrometry (figs. S5A and B) and nuclear magnetic resonance (NMR) (figs. S5C and D). Prior to use, the CL-Br was warmed to room temperature and dissolved in chloroform to 5 mg mL^{-1}. A lipid mixture of 45% POPC, 22% POPE, 8% PI, and 25% CL was used to prepare lipid vesicles mimicking the lipid composition of the mitochondrial inner membrane (IM) (*63*). Conversely, CL-enriched lipid nanotubes were prepared using a lipid ratio of 90% D-galactosyl-(β)-1,1'N-nervonoyl-D-erythro-sphingosine (C24:1 Galactosyl(β) Ceramide, GalCer), and 10% CL or CL-Br. The other lipid compositions used in this study are provided in Table S2. Vesicles and nanotubes were prepared following an established protocol (*25*). Lipid stock solutions were warmed to room temperature for 15 minutes before they were mixed in a glass vial. The lipid mixtures were dried under a stream of nitrogen with rotation, and residual chloroform was further evaporated under vacuum overnight. The lipid film was resuspended in liposome buffer containing 20 mM HEPES-NaOH, pH 7.5, and 150 mM NaCl and rehydrated via vortexing. Unilamellar vesicles were prepared by extruding the rehydrated lipid film through a 50 nm pore-size polycarbonate membrane (Avanti), flash-frozen in liquid nitrogen, aliquoted, and stored at -80 °C. Lipid nanotubes were resuspended in liposome buffer with vortexing, sonicated with a bath-sonicator at 50 °C for 3-5 minutes until the lipid clumps are dissolved, and were used immediately.

Reconstitution assays and negative-stain transmission electron microscopy (TEM).
To set up reconstitution assays, the protein samples were further purified using a Superose 6 Increase 10/300 GL column (Cytiva) equilibrated with the reaction buffer (20 mM HEPES-NaOH, pH 7.5, 130 mM NaCl, 10 mM KCl, 2 mM $MgCl_2$, 2 mM DTT, and 2% (v/v) glycerol). Purified samples (1.6 to 6 μM) were reconstituted with various liposomes (Table S2) in the presence of 500 μM β,γ-methyleneguanosine 5′-triphosphate sodium salt (GMPPCP) for 4 hours at room temperature. Reconstituted samples were applied onto a glow-discharged metal mesh grid coated with carbon and stained with uranyl formate (0.75% w/v). Samples were visualized using negative-stain TEM. Images were collected on a Tecnai T12 Spirit microscope operating at 100 kV and equipped with an AMT 2k x 2k side-mounted CCD camera. Most images were recorded at a nominal magnification of 98,000x with a calibrated pixel size of 6.47 Å/pixel.

Liposome co-sedimentation assays.
Purified wild-type or mutant S-OPA1 proteins were buffer exchanged into the liposome buffer (20 mM HEPES-NaOH, pH 7.5 and 150 mM NaCl) using micro-spin desalting columns (Thermo Scientific Zeba). Equal volumes (25 μl) of protein (0.2 to 0.25 mg ml^{-1}) and unilamellar vesicles (1.0 mg ml^{-1}) were then mixed and incubated at room temperature for 30 min. After incubation, the samples were centrifuged at 55,000 rpm for 30 min at 20 °C using a TLA-120.2 rotor (Beckman Coulter). Reaction mixtures containing liposomes without CL were centrifuged at 85,000 rpm for 30 min to pellet proteoliposomes. The resulting supernatant and pellet fractions were subjected to SDS-PAGE analysis and gel bands were quantified using ImageJ software (*64*). Lipid compositions used in co-sedimentation assays are listed in Table S2. All experiments were performed in triplicates, and error bars indicate the standard error of the mean (s.e.m.).

CryoEM grid preparation and data collection.
For cryoEM, 6 μl of membrane reconstitution reaction containing lipid nanotubes with CL-Br was pipetted onto glow-discharged R1.2/1.3 200 copper mesh grids (Quantifold) in 100% humidity at 10 °C, incubated for 30 seconds, and blotted with a blot force of 0 for 4 seconds using a Vitrobot

Mark IV (FEI). The grids were then plunge frozen into liquid ethane and stored under liquid nitrogen until imaged. Micrographs were acquired on a Titan Krios TEM (Thermo Fisher Scientific) operated at 300 kV and equipped with a K3 direct electron detector (Gatan) and a GIF Quantum energy filter (Gatan) with a slit width of 20 eV. SerialEM software (*65*) was used for data acquisition. A total of 4,640 movie stacks were acquired with a defocus range of 0.5 to 1.5 μm at a nominal magnification of 105,000x corresponding to a 0.417 Å/pixel in super-resolution mode. The movies were dose-fractionated into 118 frames with ~0.55 e^- per $Å^{-2}$ per frame and a total exposure time of 6 s, resulting in an accumulated dose of ~65 $e^-Å^{-2}$ for each stack.

CryoEM data processing and 3D Reconstruction.

Data processing procedure for membrane-bound OPA1 filaments was previously described (*10*). Briefly, motion corrected movies were imported into RELION 4.0 (*56*) and contrast transfer function (CTF) parameters were determined using CTFFIND4 (*66*). Following manual filament picking, a total of 233,341 segments were extracted from 4,640 micrographs with the data 2x binned by Fourier cropping (1.668 Å/pixel) and were subjected to multiple rounds of 2D and 3D classification, resulting in a subset of 11,469 particles. The resulting class was then subjected to 3D auto-refinement using a protein-only soft mask. Successive rounds of refinement were performed with higher resolution reference maps obtained after CTF and aberration refinements, which improved the map resolution to 6.7 Å. The helical parameters were refined to a rise of 7.69 Å and a twist of 128.642° per subunit. To further improve the signal-to-noise ratio, each independent half-map was segmented, resampled on a common grid, and summed according to the C2 symmetry axis of the OPA1 dimer using UCSF Chimera (*67*). These summed unfiltered half maps were used during the post-processing step, yielding a final reconstruction at 6.4 Å resolution. The resolution of the final reconstructions was estimated by the Fourier Shell Correlation (FSC) between the two independent half maps at FSC=0.143. Resolution-dependent negative B-factors were applied to all final reconstructions for sharpening. Local resolution estimations were calculated using ResMap (*68*). All cryo-EM data processing and analysis software was compiled and supported by the SBGrid Consortium (*69*). An overview of cryo-EM data collection and image processing statistics was provided in fig. S7.

Model building, refinement, and validation.

The cryoEM structure of membrane-bound S-OPA1 polymer (PDB ID: 8CT1) served as an initial reference for model building and refinement. Two distinct tetrameric models were extracted from the polymeric assembly and manually fitted into the density map using Chimera (*67*). The tetrameric models underwent iterative refinement against the cryoEM map with global minimization, local grid search, and B factor refinement along with secondary structure, Ramachandran, and rotamer restraints to improve the model-map correlation coefficient using the phenix.real_space_refine tool in the PHENIX software package (*70*). Further corrections to the models were made in Coot (*71*) with torsion, planar peptide, and Ramachandran restraints. The quality of the model stereochemistry was validated by PHENIX and MolProbity (*72*) and the model refinement and validation statistics are summarized in table S1. All structural figures were prepared in VMD (*73*).

Molecular dynamics simulations.

CryoEM structures of membrane-bound S-OPA1 polymers (PDB IDs: 8CT1 and 8CT9) were used as starting monomeric and tetrameric models for both CG and AA MD simulations. All MD simulation systems were setup using modules of the CHARMM-GUI server (*74*), and then minimized, equilibrated and run for production using standard CHARMM-GUI procedures, using Gromacs 2022 (*75*). Coarse-grained systems were prepared with MARTINI22p parameters and elastic networks (*76*, *77*) for POPC, POPE, and CL, all inside the corresponding CHARMM-GUI

module (*78*), except for manual building and parametrization of MLCL membranes, which along with AA MD simulation files were kindly provided by Dr. Eric May and described previously (*62*). The dimensions of membranes for CG simulations were sized around 30nm x 30nm x 27nm, reaching around 1 million beads which represent ~10 million atoms in each system. MARTINI simulations were run for production at 303 K and 1 atm following minimization and thermal equilibration by using the standard procedures and parameters as provided by CHARMM-GUI. Briefly, standard semi-isotropic Berendsen barostat was used for equilibration while progressively releasing positional restraints on the protein and standard Parrinello-Rahman semi-isotropic barostat was used without restraints. The integration timestep during production was 20 fs. The simulations were run for at least ~8 μs, with the first few microseconds of trajectories were removed for several analyses to obtain data computed on equilibrated systems.

Systems for atomistic simulations were prepared with CHARMM-GUI applying CHARMM36m parameters with the corresponding modified TIP3P (*79*). The model membranes mimicking the lipid composition of the mitochondrial inner membrane (~17% CL or MLCL, 44% POPC, and 39% POPE) was utilized in AA MD simulations and described previously (*26*). System size was ~20 nm x 20 nm x 20 nm and included over 600,000 particles. After minimization and equilibration to 303 K and 1 atm, production simulations were run using standard parameters as provided by CHARMM-GUI (standard semi-isotropic Berendsen barostat for equilibration while progressively releasing positional restraints on the protein and standard Parrinello-Rahman semi-isotropic barostat with a Nose-Hoover thermostat without restraints). PME electrostatics and a force-switch cut-off of 1 nm was applied and an integration timestep of 2 fs was used during production for around 1 μs. Analyses were performed on the second half of the production phase to probe the equilibrated systems, a crucial step due to the slow convergence of lipid diffusion in AA MD simulations.

MD trajectories were visually inspected in VMD (*73*) and analyzed with freely available tools and packages, detailed as follows. Atom-atom and bead-bead contacts were computed with tools from the PDB manipulation suite (https://lucianoabriata.altervista.org/pdbms/) applying 4 Å cutoff on non-hydrogen atoms in atomistic simulations and 8 Å cutoffs for beads in CG simulations. Minimal distances between proteins and membranes were also measured with tools from the PDB manipulation suite. Residue-wise residence times per lipid were computed with the PyLipID package (*80*) using standard settings. Volumes describing atom or bead densities were computed and visualized in VMD using the VolMap plugin, considering all non-hydrogen atoms when analyzing atomistic simulations and all beads when analyzing CG simulations. Membrane deformation was computed with the MembraneCurvature plugin for MDAnalysis, with standard settings and x,y grids of 14x14 tiles for tetramers 1 and 3 and 18x18 tiles for tetramers 2 and 4, which required a larger membrane surface. Furthermore, the trajectories for the membrane deformation analysis were processed with Gromacs' trjconv command, which centers the protein in the membrane by wrapping the frames and removes any translation and rotation on the x,y plane.

Acknowledgments

We thank Garry Morgan and Sarah Zimmermann at the EM Services Core Facility of the University of Colorado Boulder for electron microscopy training and support; the Shared Instrument Pool (SIP) core facility (RRID: SCR_018986) of the Department of Biochemistry at the University of Colorado Boulder for the use of the shared research instrumentation infrastructure; Dr. Annette Erbse for assistance with biophysical instruments and support; Lucero Castorena Casillas and Gabriella May Sullivan for carefully reading and editing the manuscript. We would also like to thank Dr. Eric May for sharing files for MD simulation analysis.

Funding

This work was supported in part by American Heart Association Postdoctoral Fellowship 23POST1020756 (K.E.Z.), Boettcher Foundation Webb-Waring Biomedical Research Award (H.A.), a National Institute of Health grant R35 GM150942 (H.A.), a National Institute of Health grant R01 GM127673 (A.F.), a Faculty Scholar Grant from the HHMI (A.F.). A.F. is an alumni investigator of the Chan Zuckerburg Biohub. LAA and MDP acknowledge the Swiss National Science Foundation (SNSF) for support and the Swiss National Supercomputing Centre (CSCS) for HPC resources, Switzerland.

Author Contributions

K.E.Z performed cloning, mutagenesis, biochemical and biophysical characterizations. F.R.M. synthesized brominated cardiolipin for cryoEM experiments and assisted with data collection. K.E.Z and F.R.M prepared liposomes for both biochemical and biophysical experiments. K.E.Z. and H.A. determine the cryoEM structures and conducted model building, refinement, and validation of the cryoEM structures. L.A.A and M.D.P performed and analyzed the molecular dynamics simulations. All authors analyzed the data, discussed the results, and wrote the manuscript.

Competing Interest Statement

A.F. and F.R.M. are shareholders and employees of Altos Labs.

References

1. P. van Bergeijk, C. C. Hoogenraad, L. C. Kapitein, Right Time, Right Place: Probing the Functions of Organelle Positioning. *Trends in Cell Biology* **26**, 121–134 (2016).
2. M. Giacomello, A. Pyakurel, C. Glytsou, L. Scorrano, The cell biology of mitochondrial membrane dynamics. *Nat Rev Mol Cell Biol* **21**, 204–224 (2020).
3. J. C. Iovine, S. M. Claypool, N. N. Alder, Mitochondrial compartmentalization: emerging themes in structure and function. *Trends in Biochemical Sciences* **46**, 902–917 (2021).
4. N. Pfanner, B. Warscheid, N. Wiedemann, Mitochondrial proteins: from biogenesis to functional networks. *Nat Rev Mol Cell Biol* **20**, 267–284 (2019).
5. A. S. Monzel, J. A. Enríquez, M. Picard, Multifaceted mitochondria: moving mitochondrial science beyond function and dysfunction. *Nat Metab* **5**, 546–562 (2023).
6. V. Eisner, M. Picard, G. Hajnoczky, Mitochondrial dynamics in adaptive and maladaptive cellular stress responses. *Nat Cell Biol* **20**, 755–765 (2018).
7. A. Liu, F. Kage, A. F. Abdulkareem, M. P. Aguirre-Huamani, G. Sapp, H. Aydin, H. N. Higgs, Fatty acyl-coenzyme A activates mitochondrial division through oligomerization of MiD49 and MiD51. *Nat Cell Biol*, 1–14 (2024).
8. R. Kalia, R. Y.-R. Wang, A. Yusuf, P. V. Thomas, D. A. Agard, J. M. Shaw, A. Frost, Structural basis of mitochondrial receptor binding and constriction by DRP1. *Nature* **558**, 401–405 (2018).
9. Y.-L. Cao, S. Meng, Y. Chen, J.-X. Feng, D.-D. Gu, B. Yu, Y.-J. Li, J.-Y. Yang, S. Liao, D. C. Chan, S. Gao, MFN1 structures reveal nucleotide-triggered dimerization critical for mitochondrial fusion. *Nature* **542**, 372–376 (2017).
10. A. von der Malsburg, G. M. Sapp, K. E. Zuccaro, A. von Appen, F. R. Moss, R. Kalia, J. A. Bennett, L. A. Abriata, M. Dal Peraro, M. van der Laan, A. Frost, H. Aydin, Structural mechanism of mitochondrial membrane remodelling by human OPA1. *Nature* **620**, 1101–1108 (2023).
11. S. B. Nyenhuis, X. Wu, M.-P. Strub, Y.-I. Yim, A. E. Stanton, V. Baena, Z. A. Syed, B. Canagarajah, J. A. Hammer, J. E. Hinshaw, OPA1 helical structures give perspective to mitochondrial dysfunction. *Nature* **620**, 1109–1116 (2023).
12. S. L. Archer, Mitochondrial Dynamics — Mitochondrial Fission and Fusion in Human Diseases. *N Engl J Med* **369**, 2236–2251 (2013).
13. J. Comte, B. Maïsterrena, D. C. Gautheron, Lipid composition and protein profiles of outer and inner membranes from pig heart mitochondria. Comparison with microsomes. *Biochimica et Biophysica Acta (BBA) - Biomembranes* **419**, 271–284 (1976).
14. S. E. Horvath, G. Daum, Lipids of mitochondria. *Progress in Lipid Research* **52**, 590–614 (2013).
15. S. T. Ahmadpour, K. Mahéo, S. Servais, L. Brisson, J.-F. Dumas, Cardiolipin, the Mitochondrial Signature Lipid: Implication in Cancer. *IJMS* **21**, 8031 (2020).
16. M. Schlame, Cardiolipin remodeling and the function of tafazzin. *Biochimica et Biophysica Acta (BBA) - Molecular and Cell Biology of Lipids* **1831**, 582–588 (2013).
17. C. U. Mårtensson, K. N. Doan, T. Becker, Effects of lipids on mitochondrial functions. *Biochimica et Biophysica Acta (BBA) - Molecular and Cell Biology of Lipids* **1862**, 102–113 (2017).
18. E. Zinser, C. D. Sperka-Gottlieb, E. V. Fasch, S. D. Kohlwein, F. Paltauf, G. Daum, Phospholipid synthesis and lipid composition of subcellular membranes in the unicellular eukaryote Saccharomyces cerevisiae. *J Bacteriol* **173**, 2026–2034 (1991).
19. J. A. Mayr, Lipid metabolism in mitochondrial membranes. *J Inherit Metab Dis* **38**, 137–144 (2015).

20. T. Ban, J. A. W. Heymann, Z. Song, J. E. Hinshaw, D. C. Chan, OPA1 disease alleles causing dominant optic atrophy have defects in cardiolipin-stimulated GTP hydrolysis and membrane tubulation. *Human Molecular Genetics* **19**, 2113–2122 (2010).
21. M. Schlame, M. Ren, The role of cardiolipin in the structural organization of mitochondrial membranes. *Biochimica et Biophysica Acta (BBA) - Biomembranes* **1788**, 2080–2083 (2009).
22. I. Bustillo-Zabalbeitia, S. Montessuit, E. Raemy, G. Basañez, O. Terrones, J.-C. Martinou, Specific interaction with cardiolipin triggers functional activation of Dynamin-Related Protein 1. *PLoS One* **9**, e102738 (2014).
23. A. L. Duncan, A. J. Robinson, J. E. Walker, Cardiolipin binds selectively but transiently to conserved lysine residues in the rotor of metazoan ATP synthases. *Proc. Natl. Acad. Sci. U.S.A.* **113**, 8687–8692 (2016).
24. A. Jussupow, A. Di Luca, V. R. I. Kaila, How cardiolipin modulates the dynamics of respiratory complex I. *Sci. Adv.* **5**, eaav1850 (2019).
25. J. A. Bennett, L. R. Steward, J. Rudolph, A. P. Voss, H. Aydin, The structure of the human LACTB filament reveals the mechanisms of assembly and membrane binding. *PLoS Biol* **20**, e3001899 (2022).
26. M. Manicki, H. Aydin, L. A. Abriata, K. A. Overmyer, R. M. Guerra, J. J. Coon, M. Dal Peraro, A. Frost, D. J. Pagliarini, Structure and functionality of a multimeric human COQ7:COQ9 complex. *Mol Cell* **82**, 4307-4323 e10 (2022).
27. S. Zhu, Z. Chen, M. Zhu, Y. Shen, L. J. Leon, L. Chi, S. Spinozzi, C. Tan, Y. Gu, A. Nguyen, Y. Zhou, W. Feng, F. M. Vaz, X. Wang, A. B. Gustafsson, S. M. Evans, O. Kunfu, X. Fang, Cardiolipin Remodeling Defects Impair Mitochondrial Architecture and Function in a Murine Model of Barth Syndrome Cardiomyopathy. *Circ: Heart Failure* **14**, e008289 (2021).
28. K. Phan, Y. He, R. Pickford, S. Bhatia, J. S. Katzeff, J. R. Hodges, O. Piguet, G. M. Halliday, W. S. Kim, Uncovering pathophysiological changes in frontotemporal dementia using serum lipids. *Sci Rep* **10**, 3640 (2020).
29. V. F. Monteiro-Cardoso, M. M. Oliveira, T. Melo, M. R. M. Domingues, P. I. Moreira, E. Ferreiro, F. Peixoto, R. A. Videira, Cardiolipin profile changes are associated to the early synaptic mitochondrial dysfunction in Alzheimer's disease. *J Alzheimers Dis* **43**, 1375–1392 (2015).
30. A. B. Chaves-Filho, I. F. D. Pinto, L. S. Dantas, A. M. Xavier, A. Inague, R. L. Faria, M. H. G. Medeiros, I. Glezer, M. Y. Yoshinaga, S. Miyamoto, Alterations in lipid metabolism of spinal cord linked to amyotrophic lateral sclerosis. *Sci Rep* **9**, 11642 (2019).
31. P. G. Barth, H. R. Scholte, J. A. Berden, J. M. Van der Klei-Van Moorsel, I. E. Luyt-Houwen, E. T. Van 't Veer-Korthof, J. J. Van der Harten, M. A. Sobotka-Plojhar, An X-linked mitochondrial disease affecting cardiac muscle, skeletal muscle and neutrophil leucocytes. *J Neurol Sci* **62**, 327–55 (1983).
32. L. C. Adès, A. K. Gedeon, M. J. Wilson, M. Latham, M. W. Partington, J. C. Mulley, J. Nelson, K. Lui, D. O. Sillence, Barth syndrome: Clinical features and confirmation of gene localisation to distal Xq28. *American Journal of Medical Genetics* **45**, 327–334 (1993).
33. P. G. Barth, C. Van den Bogert, P. A. Bolhuis, H. R. Scholte, A. H. van Gennip, R. B. H. Schutgens, A. G. Ketel, X-linked cardioskeletal myopathy and neutropenia (Barth syndrome): Respiratory-chain abnormalities in cultured fibroblasts. *Journal of Inherited Metabolic Disease* **19**, 157–160 (1996).
34. A. K. Gedeon, M. J. Wilson, A. C. Colley, D. O. Sillence, J. C. Mulley, X linked fatal infantile cardiomyopathy maps to Xq28 and is possibly allelic to Barth syndrome. *Journal of Medical Genetics* **32**, 383–388 (1995).

35. M. Abe, Y. Hasegawa, M. Oku, Y. Sawada, E. Tanaka, Y. Sakai, H. Miyoshi, Mechanism for Remodeling of the Acyl Chain Composition of Cardiolipin Catalyzed by Saccharomyces cerevisiae Tafazzin. *Journal of Biological Chemistry* **291**, 15491–15502 (2016).
36. O. Sakamoto, T. Kitoh, T. Ohura, N. Ohya, K. Iinuma, Novel missense mutation (R94S) in the TAZ (G4.5) gene in a Japanese patient with Barth syndrome. *J Hum Genet* **47**, 229–231 (2002).
37. S. Vesel, M. Stopar-Obreza, K. Trebušak-Podkrajšek, J. Jazbec, T. Podnar, T. Battelino, A novel mutation in the G4.5 (TAZ) gene in a kindred with Barth syndrome. *Eur J Hum Genet* **11**, 97–101 (2003).
38. M. Schlame, J. A. Towbin, P. M. Heerdt, R. Jehle, S. DiMauro, T. J. J. Blanck, Deficiency of tetralinoleoyl-cardiolipin in Barth syndrome. *Annals of Neurology* **51**, 634–637 (2002).
39. S. M. Claypool, J. M. McCaffery, C. M. Koehler, Mitochondrial mislocalization and altered assembly of a cluster of Barth syndrome mutant tafazzins. *J Cell Biol* **174**, 379–90 (2006).
40. N. Ikon, R. O. Ryan, Cardiolipin and mitochondrial cristae organization. *Biochim Biophys Acta Biomembr* **1859**, 1156–1163 (2017).
41. S. Kameoka, Y. Adachi, K. Okamoto, M. Iijima, H. Sesaki, Phosphatidic Acid and Cardiolipin Coordinate Mitochondrial Dynamics. *Trends in Cell Biology* **28**, 67–76 (2018).
42. A. Olichon, L. Baricault, N. Gas, E. Guillou, A. Valette, P. Belenguer, G. Lenaers, Loss of OPA1 perturbates the mitochondrial inner membrane structure and integrity, leading to cytochrome c release and apoptosis. *J Biol Chem* **278**, 7743–6 (2003).
43. L. Griparic, N. N. van der Wel, I. J. Orozco, P. J. Peters, A. M. van der Bliek, Loss of the intermembrane space protein Mgm1/OPA1 induces swelling and localized constrictions along the lengths of mitochondria. *J Biol Chem* **279**, 18792–18798 (2004).
44. S. Cipolat, O. M. de Brito, B. Dal Zilio, L. Scorrano, OPA1 requires mitofusin 1 to promote mitochondrial fusion. *Proc. Natl. Acad. Sci. U.S.A.* **101**, 15927–15932 (2004).
45. S. Cogliati, C. Frezza, M. E. Soriano, T. Varanita, R. Quintana-Cabrera, M. Corrado, S. Cipolat, V. Costa, A. Casarin, L. C. Gomes, E. Perales-Clemente, L. Salviati, P. Fernandez-Silva, J. A. Enriquez, L. Scorrano, Mitochondrial Cristae Shape Determines Respiratory Chain Supercomplexes Assembly and Respiratory Efficiency. *Cell* **155**, 160–171 (2013).
46. M. Y. Fry, P. P. Navarro, P. Hakim, V. Y. Ananda, X. Qin, J. C. Landoni, S. Rath, Z. Inde, C. M. Lugo, B. E. Luce, Y. Ge, J. L. McDonald, I. Ali, L. L. Ha, B. P. Kleinstiver, D. C. Chan, K. A. Sarosiek, L. H. Chao, In situ architecture of Opa1-dependent mitochondrial cristae remodeling. *The EMBO Journal* **43**, 391–413 (2024).
47. V. Del Dotto, P. Mishra, S. Vidoni, M. Fogazza, A. Maresca, L. Caporali, J. M. McCaffery, M. Cappelletti, E. Baruffini, G. Lenaers, D. Chan, M. Rugolo, V. Carelli, C. Zanna, OPA1 Isoforms in the Hierarchical Organization of Mitochondrial Functions. *Cell Reports* **19**, 2557–2571 (2017).
48. P. Mishra, V. Carelli, G. Manfredi, D. C. Chan, Proteolytic cleavage of Opa1 stimulates mitochondrial inner membrane fusion and couples fusion to oxidative phosphorylation. *Cell Metab* **19**, 630–41 (2014).
49. R. Anand, T. Wai, M. J. Baker, N. Kladt, A. C. Schauss, E. Rugarli, T. Langer, The i-AAA protease YME1L and OMA1 cleave OPA1 to balance mitochondrial fusion and fission. *Journal of Cell Biology* **204**, 919–929 (2014).
50. T. Ban, T. Ishihara, H. Kohno, S. Saita, A. Ichimura, K. Maenaka, T. Oka, K. Mihara, N. Ishihara, Molecular basis of selective mitochondrial fusion by heterotypic action between OPA1 and cardiolipin. *Nat Cell Biol* **19**, 856–863 (2017).
51. Y. Ge, X. Shi, S. Boopathy, J. McDonald, A. W. Smith, L. H. Chao, Two forms of Opa1 cooperate to complete fusion of the mitochondrial inner-membrane. *Elife* **9**, e50973 (2020).

52. D. Zhang, Y. Zhang, J. Ma, C. Zhu, T. Niu, W. Chen, X. Pang, Y. Zhai, F. Sun, Cryo-EM structures of S-OPA1 reveal its interactions with membrane and changes upon nucleotide binding. *eLife* **9**, e50294 (2020).
53. J. R. Jimah, J. E. Hinshaw, Structural Insights into the Mechanism of Dynamin Superfamily Proteins. *Trends in Cell Biology* **29**, 257–273 (2019).
54. F. R. Moss, J. Lincoff, M. Tucker, A. Mohammed, M. Grabe, A. Frost, Brominated lipid probes expose structural asymmetries in constricted membranes. *Nat Struct Mol Biol* **30**, 167–175 (2023).
55. W. R. Arnold, A. Mancino, F. R. Moss, A. Frost, D. Julius, Y. Cheng, Structural basis of TRPV1 modulation by endogenous bioactive lipids. *Nat Struct Mol Biol*, 1–9 (2024).
56. D. Kimanius, L. Dong, G. Sharov, T. Nakane, S. H. W. Scheres, New tools for automated cryo-EM single-particle analysis in RELION-4.0. *Biochem J* **478**, 4169–4185 (2021).
57. J. M. East, A. G. Lee, Lipid selectivity of the calcium and magnesium ion dependent adenosinetriphosphatase, studied with fluorescence quenching by a brominated phospholipid. *Biochemistry* **21**, 4144–51 (1982).
58. K. Hristova, S. H. White, Determination of the hydrocarbon core structure of fluid dioleoylphosphocholine (DOPC) bilayers by x-ray diffraction using specific bromination of the double-bonds: effect of hydration. *Biophys J* **74**, 2419–33 (1998).
59. D. Persson, P. E. G. Thorén, E. K. Esbjörner, M. Goksör, P. Lincoln, B. Nordén, Vesicle size-dependent translocation of penetratin analogs across lipid membranes. *Biochimica et Biophysica Acta (BBA) - Biomembranes* **1665**, 142–155 (2004).
60. A. L. Duncan, Monolysocardiolipin (MLCL) interactions with mitochondrial membrane proteins. *Biochemical Society Transactions* **48**, 993–1004 (2020).
61. G. L. Powell, D. Marsh, Polymorphic phase behavior of cardiolipin derivatives studied by phosphorus-31 NMR and x-ray diffraction. *Biochemistry* **24**, 2902–2908 (1985).
62. K. J. Boyd, N. N. Alder, E. R. May, Molecular Dynamics Analysis of Cardiolipin and Monolysocardiolipin on Bilayer Properties. *Biophysical Journal* **114**, 2116–2127 (2018).
63. D. Ardail, J. P. Privat, M. Egret-Charlier, C. Levrat, F. Lerme, P. Louisot, Mitochondrial contact sites. Lipid composition and dynamics. *Journal of Biological Chemistry* **265**, 18797–18802 (1990).
64. J. Schindelin, I. Arganda-Carreras, E. Frise, V. Kaynig, M. Longair, T. Pietzsch, S. Preibisch, C. Rueden, S. Saalfeld, B. Schmid, J. Y. Tinevez, D. J. White, V. Hartenstein, K. Eliceiri, P. Tomancak, A. Cardona, Fiji: an open-source platform for biological-image analysis. *Nat Methods* **9**, 676–82 (2012).
65. D. N. Mastronarde, Automated electron microscope tomography using robust prediction of specimen movements. *J Struct Biol* **152**, 36–51 (2005).
66. A. Rohou, N. Grigorieff, CTFFIND4: Fast and accurate defocus estimation from electron micrographs. *Journal of Structural Biology* **192**, 216–221 (2015).
67. E. F. Pettersen, T. D. Goddard, C. C. Huang, G. S. Couch, D. M. Greenblatt, E. C. Meng, T. E. Ferrin, UCSF Chimera--a visualization system for exploratory research and analysis. *J Comput Chem* **25**, 1605–12 (2004).
68. A. Kucukelbir, F. J. Sigworth, H. D. Tagare, Quantifying the local resolution of cryo-EM density maps. *Nat Methods* **11**, 63–5 (2014).
69. A. Morin, B. Eisenbraun, J. Key, P. C. Sanschagrin, M. A. Timony, M. Ottaviano, P. Sliz, Collaboration gets the most out of software. *Elife* **2**, e01456 (2013).
70. D. Liebschner, P. V. Afonine, M. L. Baker, G. Bunkóczi, V. B. Chen, T. I. Croll, B. Hintze, L.-W. Hung, S. Jain, A. J. McCoy, N. W. Moriarty, R. D. Oeffner, B. K. Poon, M. G. Prisant, R. J. Read, J. S. Richardson, D. C. Richardson, M. D. Sammito, O. V. Sobolev, D. H. Stockwell, T. C. Terwilliger, A. G. Urzhumtsev, L. L. Videau, C. J. Williams, P. D. Adams,

Macromolecular structure determination using X-rays, neutrons and electrons: recent developments in *Phenix*. *Acta Crystallogr D Struct Biol* **75**, 861–877 (2019).

71. P. Emsley, B. Lohkamp, W. G. Scott, K. Cowtan, Features and development of *Coot*. *Acta Crystallogr D Biol Crystallogr* **66**, 486–501 (2010).
72. C. J. Williams, J. J. Headd, N. W. Moriarty, M. G. Prisant, L. L. Videau, L. N. Deis, V. Verma, D. A. Keedy, B. J. Hintze, V. B. Chen, S. Jain, S. M. Lewis, W. B. Arendall, J. Snoeyink, P. D. Adams, S. C. Lovell, J. S. Richardson, D. C. Richardson, MolProbity: More and better reference data for improved all-atom structure validation. *Protein Science* **27**, 293–315 (2018).
73. W. Humphrey, A. Dalke, K. Schulten, VMD: visual molecular dynamics. *J Mol Graph* **14**, 33–8, 27–8 (1996).
74. S. Jo, T. Kim, V. G. Iyer, W. Im, CHARMM-GUI: a web-based graphical user interface for CHARMM. *J Comput Chem* **29**, 1859–65 (2008).
75. P. Bauer, B. Hess, E. Lindahl, Gromacs 2022 Manual. doi: 10.5281/zenodo.6103568 (2022).
76. D. H. de Jong, G. Singh, W. F. Bennett, C. Arnarez, T. A. Wassenaar, L. V. Schafer, X. Periole, D. P. Tieleman, S. J. Marrink, Improved Parameters for the Martini Coarse-Grained Protein Force Field. *J Chem Theory Comput* **9**, 687–97 (2013).
77. X. Periole, M. Cavalli, S. J. Marrink, M. A. Ceruso, Combining an Elastic Network With a Coarse-Grained Molecular Force Field: Structure, Dynamics, and Intermolecular Recognition. *J Chem Theory Comput* **5**, 2531–43 (2009).
78. Y. Qi, H. I. Ingolfsson, X. Cheng, J. Lee, S. J. Marrink, W. Im, CHARMM-GUI Martini Maker for Coarse-Grained Simulations with the Martini Force Field. *J Chem Theory Comput* **11**, 4486–94 (2015).
79. J. Huang, S. Rauscher, G. Nawrocki, T. Ran, M. Feig, B. L. de Groot, H. Grubmuller, A. D. MacKerell, CHARMM36m: an improved force field for folded and intrinsically disordered proteins. *Nat Methods* **14**, 71–73 (2017).
80. W. Song, R. A. Corey, T. B. Ansell, C. K. Cassidy, M. R. Horrell, A. L. Duncan, P. J. Stansfeld, M. S. P. Sansom, PyLipID: A Python Package for Analysis of Protein-Lipid Interactions from Molecular Dynamics Simulations. *J Chem Theory Comput* **18**, 1188–1201 (2022).

Figure Legends

Figure 1. Interactions between lipids and S-OPA1 residues and changes in membrane topology. (A) The S-OPA1 tetramer model was extracted from the cryoEM structure of the membrane-bound S-OPA1 polymer in membrane-proximal conformation (PDB ID: 8CT1) and fitted into cryoEM density map (EMDB ID: 26977). Each subunit of the tetramer is shown in surface representation and different colors. The extracted ribbon model for S-OPA1 monomer is colored in orange (GTPase), red (BSE), blue (stalk), and green (PD) to highlight the domain organization of S-OPA1 and the surface is depicted as semi-transparent solid density. IL, Inner Leaflet; OL, Outer Leaflet; PL, Protein Layer. **(B)** The CG MD simulations for tetramer 1 docked on a membrane containing 20% CL, 40% POPC and 40% POPE and relaxed through the several microsecond simulations. Each OPA1 monomer is shown in surface representation with a different color. The panel displays the trajectory-averaged density of lipid headgroup beads and the slight average curvature experienced by the membrane. The density for all CL beads is colored in magenta and indicate the clustering of CL molecules at the protein-membrane contact sites. Top (1) and bottom (2) views of the S-OPA1 tetramer simulated on CL-enriched membranes. **(C)** Residence times for contacts between protein and lipid beads are shown for CL, POPE and POPC and are calculated for all four subunits in each of the three CG MD simulation replicates for tetramer 1. The red regions within the tetrameric model indicate the position of the PD residues with longer residence times. **(D)** Average number of protein-lipid contacts per residue were calculated using the last 300 ns of the AA MD simulations in 3 independent replicas. **(E)** AA MD simulations show average CL density clustering near protein-membrane contact sites. The simulations were set up by using a monomeric S-OPA1 model extracted from the tetramer 1 and membranes mimicking the lipid composition of the mitochondrial inner membrane (IM) and run in triplicates. **(F)** Membrane deformation in CG MD simulations. Mean membrane curvatures averaged throughout the last 4 μs of CG MD simulations for tetramer 1 (left) compared to a control simulation without protein. The dashed lines indicate the position of the S-OPA1 tetramer shown from the top. The x and y axes indicate the dimensions of the membrane in Angstroms. **(G)** The trajectories of OPA1-membrane interactions using S-OPA1 starting model positioned ~60 Å away from the membrane. The graph shows the minimal distance between the protein and membrane, calculated from five independent replicas of the simulation (left). The heat map was generated using one of the replicas that shows strong binding to the membrane and displays the number of membrane contacts for S-OPA1 residues over time (nanoseconds).

Figure 2. Characterization of key membrane interface residues. (A) The SDS-PAGE analysis of the co-sedimentation assays with S-OPA1 WT, MIL mutant, R857A, and R858A in the presence and absence of CL-containing liposomes. S, supernatant. P, pellet. **(B)** The quantification of the bands corresponding to S and P fractions were performed using ImageJ and unpaired two-tailed student T test was calculated from n=3 independent experiments for all data points. The asterisk(s) above the bars indicate the following: $P<0.0001$ (****), $P<0.001$ to $P>0.0001$ (***), $P<0.005$ to $P>0.001$ (**), $P<0.05$ to $P>0.005$ (*), and $P>0.05$ (not significant, ns). **(C)** The reconstitution assays for WT and mutant S-OPA1 samples were visualized by negative-stain TEM. Scale bar is 100 nm.

Figure 3. CryoEM reconstruction of human S-OPA1 bound to CL-Br-enriched membranes. (A) Structure of tetrabrominated CL. **(B)** The side view for surface representation and corresponding ribbon diagram of the S-OPA1 tetramer 1 oriented into the cryoEM density map. Inset window shows the close-up view of the paddle domain (green) and conserved MIL region interacting with membranes. **(C)** Tetrameric ribbon model of the S-OPA1 bound to CL-Br membranes. The four structural domains are colored as follows: GTPase (orange), BSE (red),

Stalk (blue), and Paddle (green). **(D)** A gray scale slice of the cryoEM 3D reconstruction of the membrane-bound S-OPA1 filament. The green rectangle indicates the position of the magnified view shown in panel E. **(E)** The difference map calculated from brominated and native protein-lipid reconstructions shows additional densities (magenta) located near the PDs (green) of S-OPA1.

Figure 4. S-OPA1 interactions with MLCL-containing membranes. (A) Membrane deformation calculations are shown for one of the three independent replicas using S-OPA1 tetramer 1 and model membranes containing either 20% CL (left) or 20% MLCL (right). Red and blue colors indicate membrane pulling and pushing in the direction of z, respectively. The membrane deformation activity of tetramer 1, particularly its ability to push down on the sides, is reduced in the presence of MLCL. **(B)** The co-sedimentation assays with S-OPA1 WT and liposomes containing CL and increasing molar ratios of MLCL. Supernatant and pellet samples from the co-sedimentation assays were harvested after centrifugation and analyzed by SDS-PAGE. **(C)** The assays were performed in triplicates and gel images were quantified by ImageJ. An unpaired two-tailed student T test was used for statistical analysis. The asterisk(s) above the bars indicate the following: P<0.0001 (****), P<0.001 to P>0.0001(***), P<0.005 to P>0.001 (**), P<0.05 to P>0.005(*), and P>0.05 (not significant, ns). **(D)** Representative negative-stain TEM images of reconstitution assays in the presence of CL and MLCL containing liposomes. Increasing molar ratios of MLCL impairs the membrane remodeling activity of S-OPA1. Scale bars are 100 nm.

Figure 5. Proposed model of how CL controls mitochondrial remodeling. OPA1 interactions with randomly distributed CL molecules in membranes trigger the clustering of CL near protein-membrane contact sites and facilitate the remodeling of membranes. The accumulation of MLCL in membranes disrupts the membrane remodeling activity of OPA1 and causes abnormalities in mitochondrial morphology.

Supplementary Figure Legends

Figure S1. Visualize the four OPA1 tetramers used in MD and provide an overview of the setup of MD simulations. (A-C) Three tetrameric subassemblies of the S-OPA1 polymer (tetramers 2, 3, and 4) were fitted into the corresponding density map that is transparently visible. Each monomer is shown in surface representation and colored differently for clarity. Tetramer 2 **(A)** is extracted from the polymeric model in membrane-proximal conformation, while tetramers 3 **(B)** and 4 **(C)** are extracted from the polymeric model that represents the membrane-distal conformation of the S-OPA1 polymer. **(D, E)** Superimposition of the S-OPA1 tetramers assembled using different oligomerization interfaces. **(D)** Tetramers representing the conserved crisscross association of dynamin superfamily proteins. **(E)** The newly identified interface 7 mediates the formation of other tetrameric assemblies in the membrane-bound state. The root-mean-square deviation (RMSD) is calculated using the CLICK server. **(F)** A representative image of the membrane patch used CG MD simulations. The lipid molecules are shown in magenta (CL), green (POPC), and cyan (POPE) and the subunits of the S-OPA1 tetramer are colored blue, yellow, orange, and gray. The membrane-inserting loop (MIL) region is highlighted in green. S-OPA1 tetramers are positioned closely to the membrane patch in the simulations. After <1 μs simulation time, the tetramers rapidly formed charge-charge and hydrophobic interactions with the bilayer lipids and deformed the membrane patch. **(G)** The S-OPA1 tetramers containing mutations within the MIL and docking regions do not bind the membrane patch and remain in solution within the timescale of the simulations.

Figure S2. Sequence alignment of OPA1 paddle domain (PD) from various species. The sequence alignment of PD residues (736 to 860) demonstrates high sequence conservation across 33 species.

Figure S3. Membrane deformation analysis of S-OPA1 tetramer in CG MD simulations. Red and blue colors indicate membrane pulling and pushing in the direction of z, respectively. The x and y axes indicate the number of membrane tiles; each tile represents 15 Å. **(A)** Membrane deformation calculations are shown for two other independent replicas using S-OPA1 tetramer 1 and model membranes containing either 20% CL (left) or 20% MLCL (right). The membrane deformation activity of tetramer 1, particularly its ability to push down on the sides, is reduced in the presence of MLCL. **(B)** Average membrane deformation was calculated for S-OPA1 tetramers 2, 3, and 4. A comparison of CL- and MLCL-containing membranes indicates reduced membrane deformation in the presence of MLCL for tetramer 3. While the CG MD simulations with tetramers 1 and 3 display significant membrane bending with CL-containing membranes, tetramers 2 and 4 show no visible difference between the two membranes.

Figure S4. Membrane binding and remodeling experiments. (A) A representative size-exclusion chromatography (SEC) profile of S-OPA1 WT and **(B)** SDS-PAGE of S-OPA1 protein following SEC. **(C)** Membrane reconstitution assays of S-OPA1 WT using four different liposomes containing POPC, POPE, L-PI, and CL at various concentrations. The PC:PE:PI:CL liposomes contain 45% POPC, 22% POPE, 8% L-PI, and 25% CL; the PC:PE:PI liposomes contain 70% POPC, 22% POPE, and 8% L-PI; the PC:PE liposomes contains 78% POPC and 22% POPE; and the PC liposomes contain 100% POPC. The samples were incubated for ~4 hours at room temperature and visualized by using negative-stain TEM. Scale bar is 100 nm. **(D)** Co-sedimentation assays were performed with the same liposomes as in (C). Supernatant and pellet samples were collected after centrifugation, subjected to SDS-PAGE, and quantified using ImageJ. An unpaired two-tailed student T test was used for statistical analysis. The asterisk(s) above the bars indicate the following: $P<0.0001$ (****), $P<0.001$ to $P>0.0001$(***), $P<0.005$ to $P>0.001$ (**), $P<0.05$ to $P>0.005$(*), and $P>0.05$ (not significant, ns).

Figure S5. Validation of brominated cardiolipin. (A) Mass spectrum of brominated cardiolipin from 780 to 1280 mass to charge ratio (m/z). **(B)** Zoomed-in view of the mass spectrum from 1042 to 1052 m/z. **(C, D)** The brominated cardiolipin chemistry was validated by small ligand NMR. The NMR Spectrum of cardiolipin H^1 **(C)** and brominated cardiolipin H^1 **(D)**. **(E)** Representative negative-stain TEM images of reconstitution assays show cylindrical and spherical liposomes in the presence and absence of S-OPA1 WT. Protein samples bind and form higher-order assemblies on brominated and native liposomes. Scale bar is 100 nm.

Figure S6. CryoEM imaging and image analysis of S-OPA1 assemblies bound to brominated liposomes. (A) Electron cryo-micrograph showing S-OPA1 filaments assembled on liposomes containing CL-Br. **(B)** Representative 2D class averages of S-OPA1 filament segments. **(C)** Gold-standard Fourier Shell Correlation (FSC) curve of the final density map. **(D)** Local resolution estimates for the cryoEM 3D reconstruction. Both horizontal and vertical slices through cryo-EM densities are shown. **(E)** S-OPA1 tetramer bound to brominated nanotubes (colored) superimposed with the tetrameric model bound to native nanotubes (gray) show minimal structural differences between the two models.

Figure S7. CryoEM data processing flowchart of S-OPA1 bound to brominated cardiolipin containing membranes. Details of cryoEM data collection and image analysis are described in the methods section.

Figure S8. Comparison of the Coulombic potentials from the resulting 3D maps of unlabeled versus bromine labeled membrane tubes. (A) A gray scale slice of along the helical axis shows CL enrichment in the outer leaflet. **(B)** Radial profiles from the cryoEM 3D reconstructions indicate the location of the surplus signals attributed to halogen scattering. The red box in panel A indicates the region used in intensity analysis. **(C)** Zoomed in view of a horizontal slice through the cryo-EM density map showing S-OPA1 monomer-membrane interactions. Dashed circles indicate the regions used in intensity measurements. **(D)** Radial profile measurements for the protein-membrane contact sites indicate the location of the surplus signals attributable to halogen scattering near the MIL region. The delta intensity is calculated by using the cryoEM 3D reconstructions of native and brominated protein-bound lipid nanotubes. **(E)** A gray scale slice of the difference map of S-OPA1 polymer bound to native and brominated liposomes shows CL enrichment in the outer leaflet. IL, Inner Leaflet; OL, Outer Leaflet; PD, Paddle Domain.

Figure S9. Comparison of residence times for CL and MLCL lipids in AA and CG MD simulations. (A) Residence times for contacts between S-OPA1 residues and CL (blue line) and MLCL (red line) lipids in CG MD simulations. The data was averaged over four subunits in each tetramer and three replicas. **(B)** Average number of protein-lipid contacts calculated from three replicas of AA MD simulations using S-OPA1 tetramer and CL- and MLCL-enriched membranes.

Figure S10. Negative-stain TEM images of liposomes. Different molar concentrations of CL and MLCL were used to prepare various liposomes. Electron microscopy images show similar morphology for liposomes containing increasing concentrations of MLCL compared to CL-enriched liposomes. Scale bars are 100 nm.

Table S1. Cryo-EM data collection, refinement, and validation statistics for the two tetrameric S-OPA1 models.

Table S2. List of liposome compositions used in reconstitution assays, co-sedimentation experiments, and cryoEM imaging. (A) Lipid molar concentrations of individual lipids in CL-containing liposomes. **(B)** Lipid molar concentrations of individual lipids in CL- and MLCL-containing liposomes. **(C)** The lipid composition of liposomes and nanotubes containing brominated cardiolipin (CL-Br).

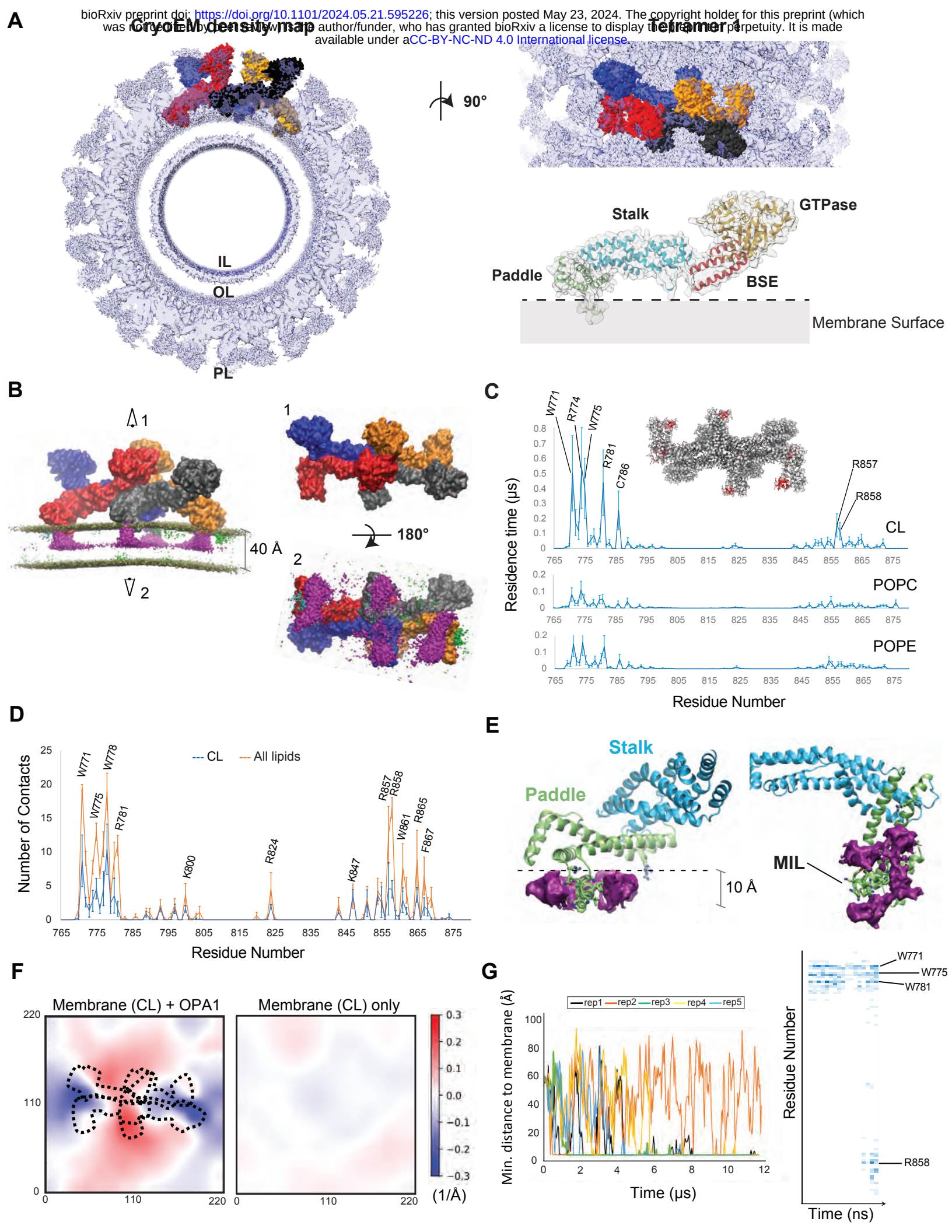

A

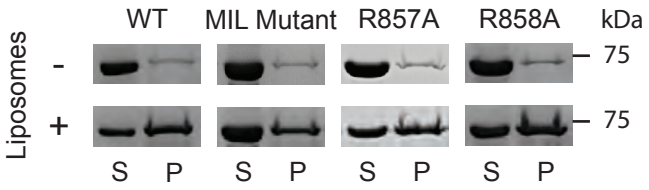

B

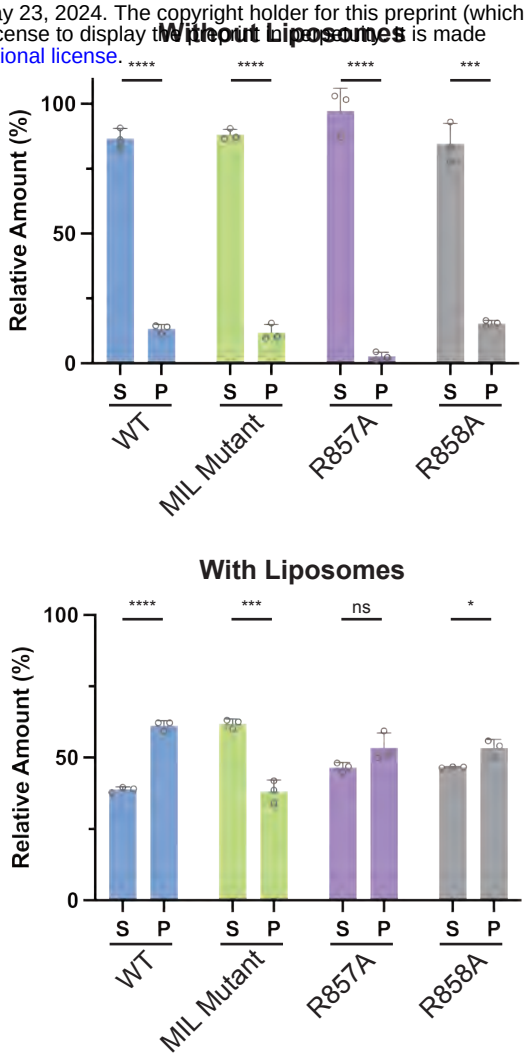

C

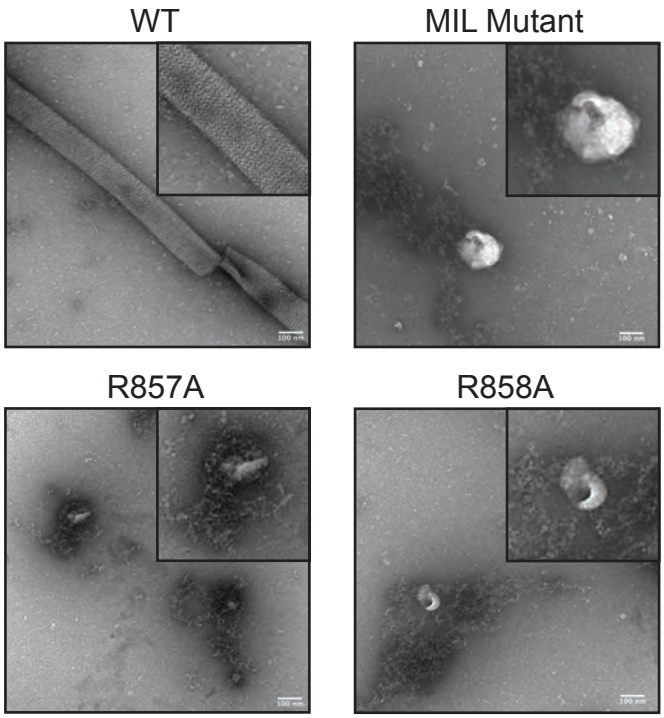

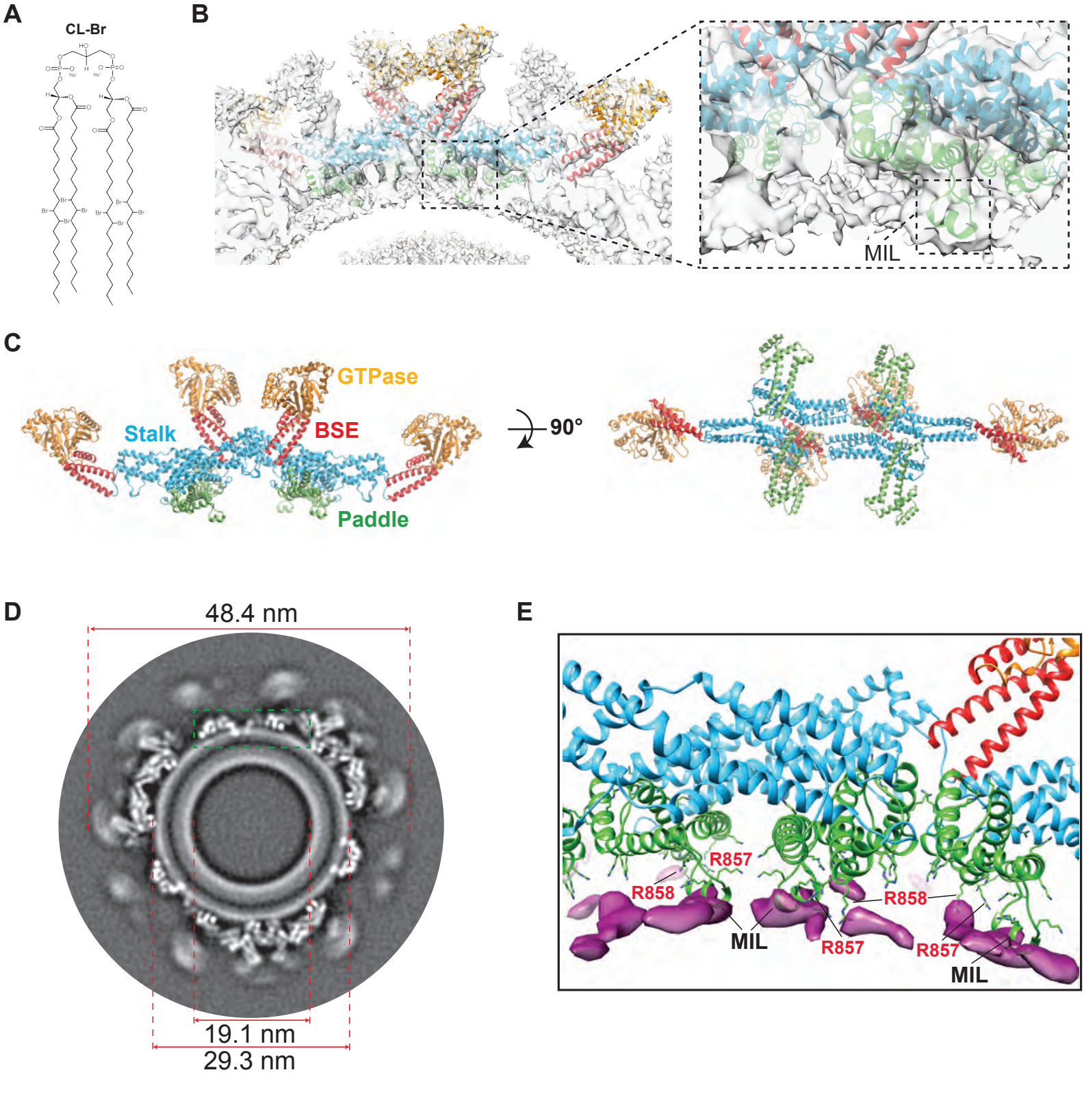

A

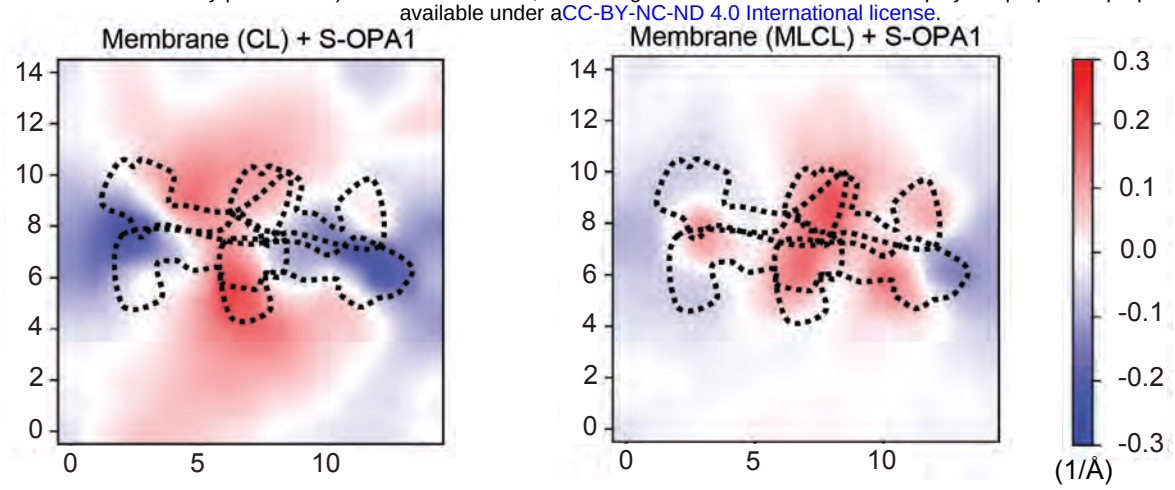

B

C

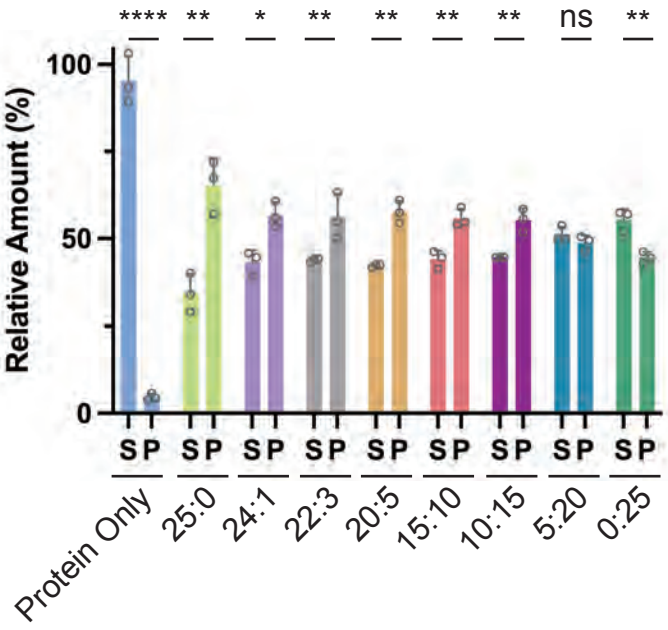

D

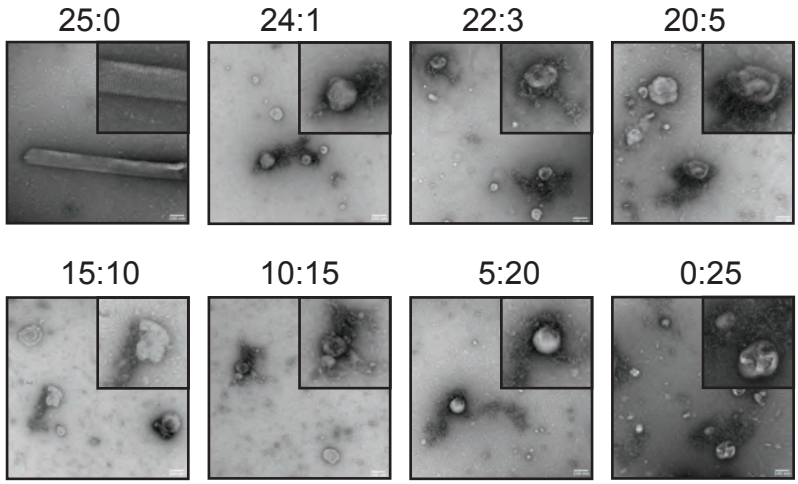

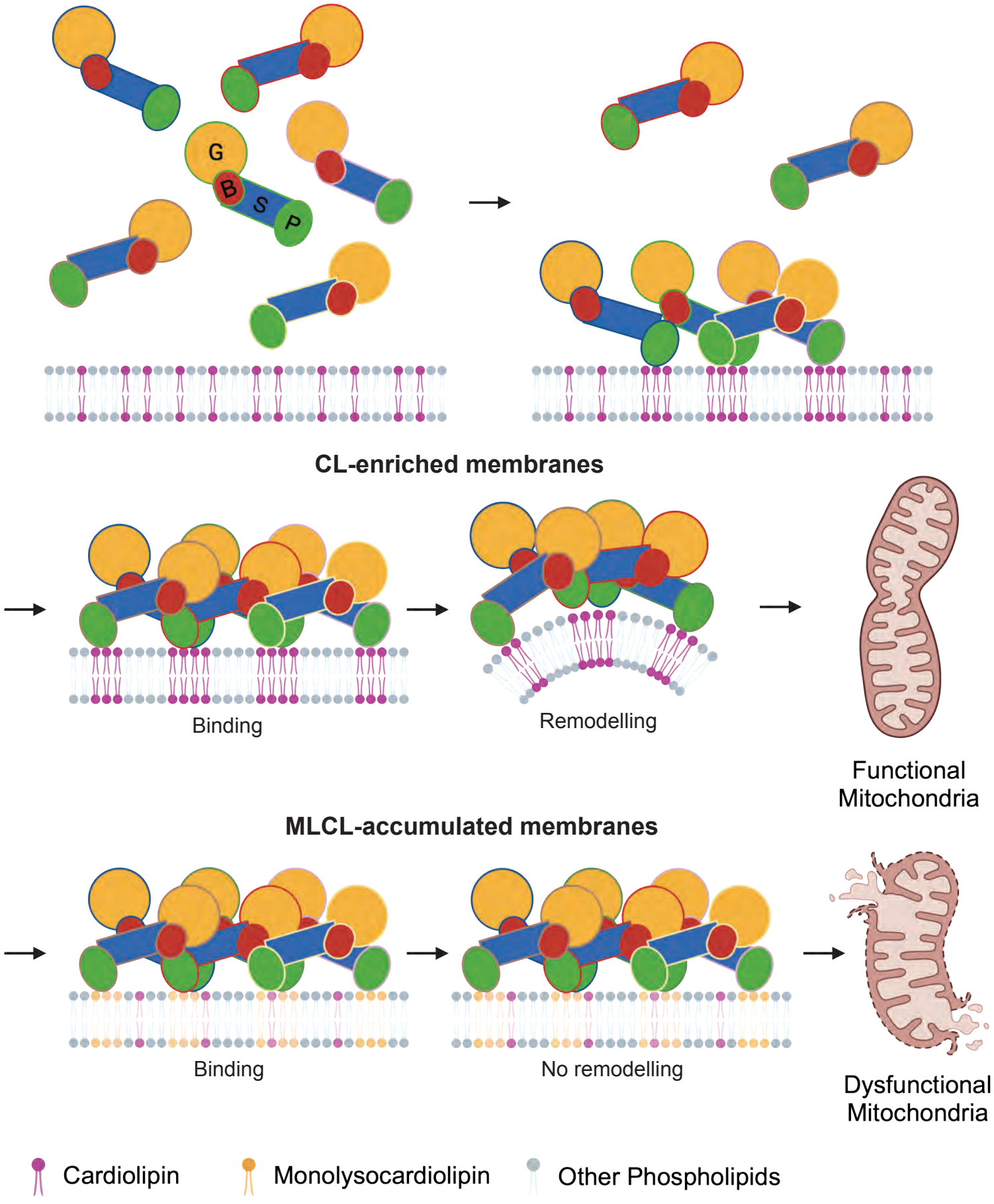

Figure S1

A

Tetramer 2

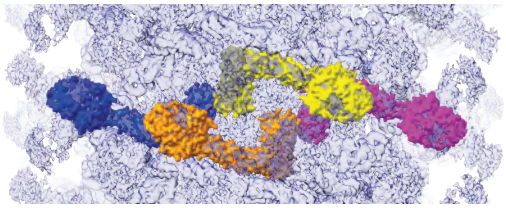

B

Tetramer 3

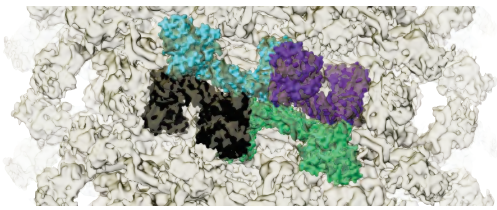

C

Tetramer 4

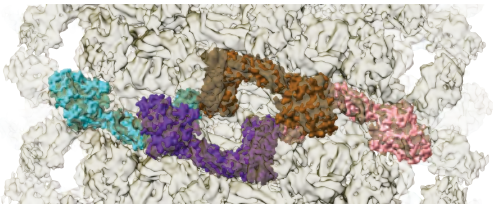

D

RMSD 2.49 Å

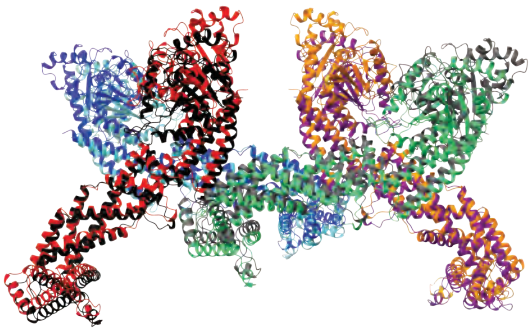

E

RMSD 2.47 Å

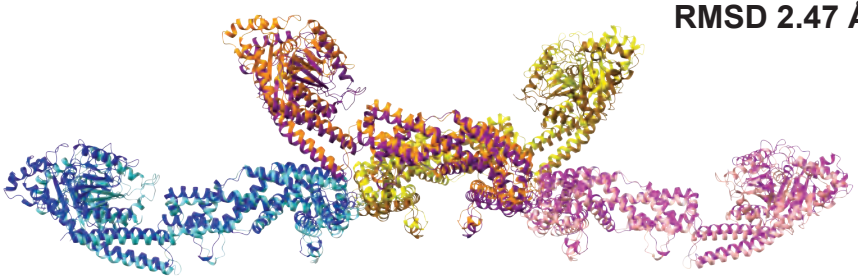

F

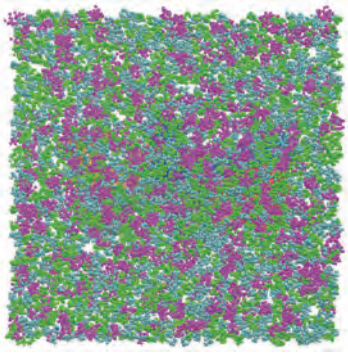

90°

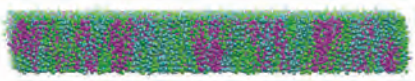

CL POPC POPE

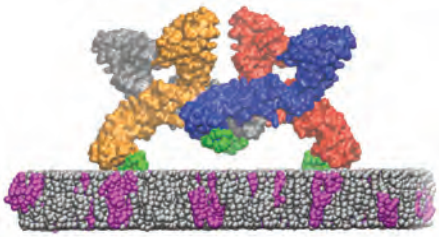

< 1 µs

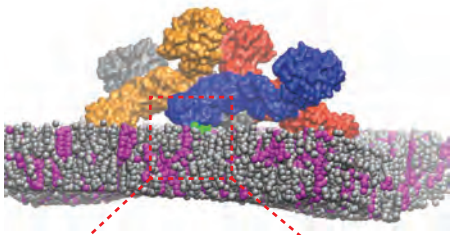

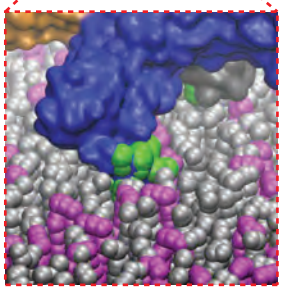

OPA1 Tetramer
in initially random lipid distribution

G

Mutant OPA1 Tetramer

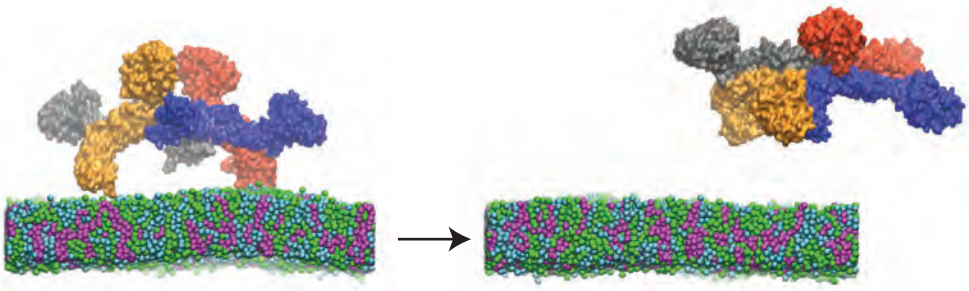

CL POPC POPE

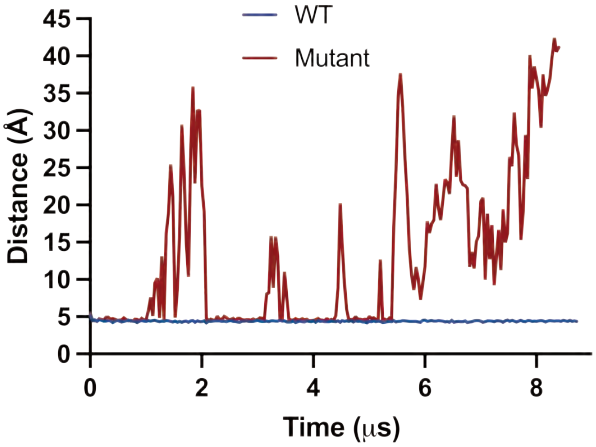

Figure S2

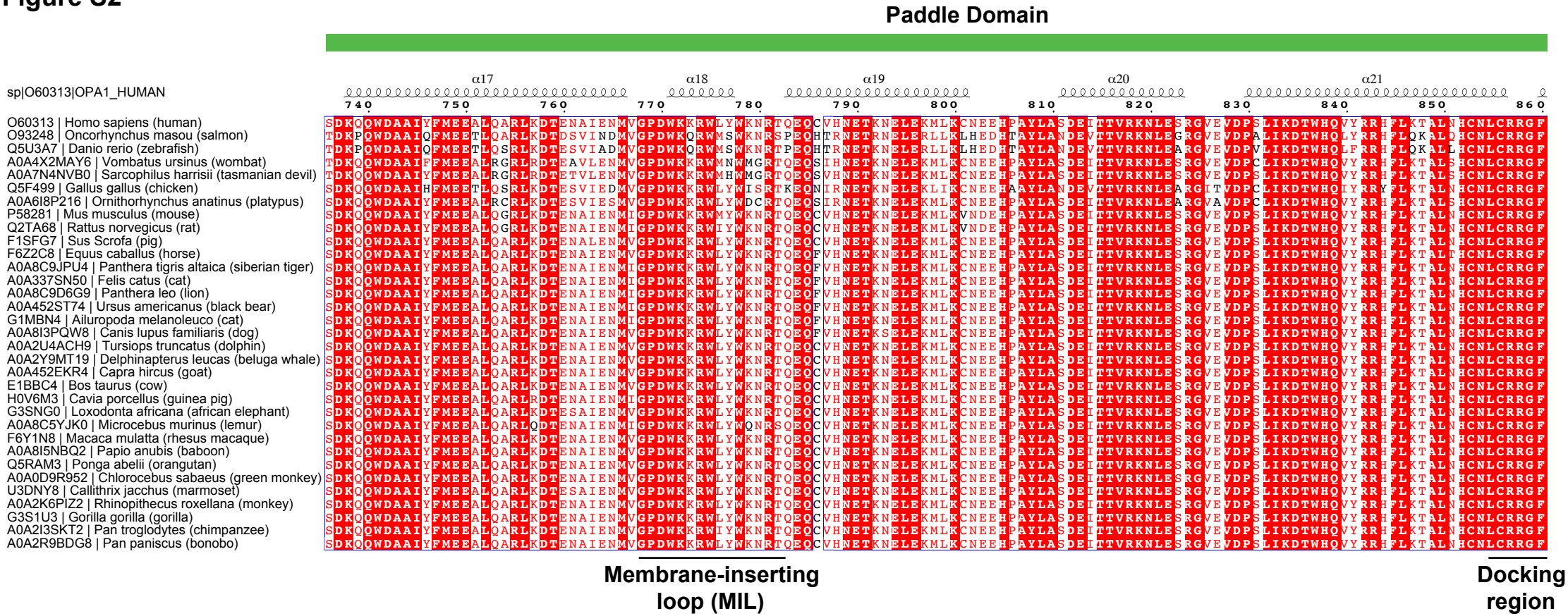
Paddle Domain
α17
α18
α19
α20
α21
sp|O60313|OPA1_HUMAN
740
750
760
770
780
790
800
810
820
830
840
850
860
O60313 | Homo sapiens (human)
O93248 | Oncorhynchus masou (salmon)
Q5U3A7 | Danio rerio (zebrafish)
A0A4X2MAY6 | Vombatus ursinus (wombat)
A0A7N4NVB0 | Sarcophilus harrisii (tasmanian devil)
Q5F499 | Gallus gallus (chicken)
A0A6I8P216 | Ornithorhynchus anatinus (platypus)
P58281 | Mus musculus (mouse)
Q2TA68 | Rattus norvegicus (rat)
F1SFG7 | Sus Scrofa (pig)
F6Z2C8 | Equus caballus (horse)
A0A8C9JPU4 | Panthera tigris altaica (siberian tiger)
A0A337SN50 | Felis catus (cat)
A0A8C9D6G9 | Panthera leo (lion)
A0A452ST74 | Ursus americanus (black bear)
G1MBN4 | Ailuropoda melanoleuco (cat)
A0A8I3PQW8 | Canis lupus familiaris (dog)
A0A2U4ACH9 | Tursiops truncatus (dolphin)
A0A2Y9MT19 | Delphinapterus leucas (beluga whale)
A0A452EKR4 | Capra hircus (goat)
E1BBC4 | Bos taurus (cow)
H0V6M3 | Cavia porcellus (guinea pig)
G3SNG0 | Loxodonta africana (african elephant)
A0A8C5YJK0 | Microcebus murinus (lemur)
F6Y1N8 | Macaca mulatta (rhesus macaque)
A0A8I5NBQ2 | Papio anubis (baboon)
Q5RAM3 | Ponga abelii (orangutan)
A0A0D9R952 | Chlorocebus sabaeus (green monkey)
U3DNY8 | Callithrix jacchus (marmoset)
A0A2K6PIZ2 | Rhinopithecus roxellana (monkey)
G3S1U3 | Gorilla gorilla (gorilla)
A0A2I3SKT2 | Pan troglodytes (chimpanzee)
A0A2R9BDG8 | Pan paniscus (bonobo)
Membrane-inserting loop (MIL)
Docking region

Figure S3

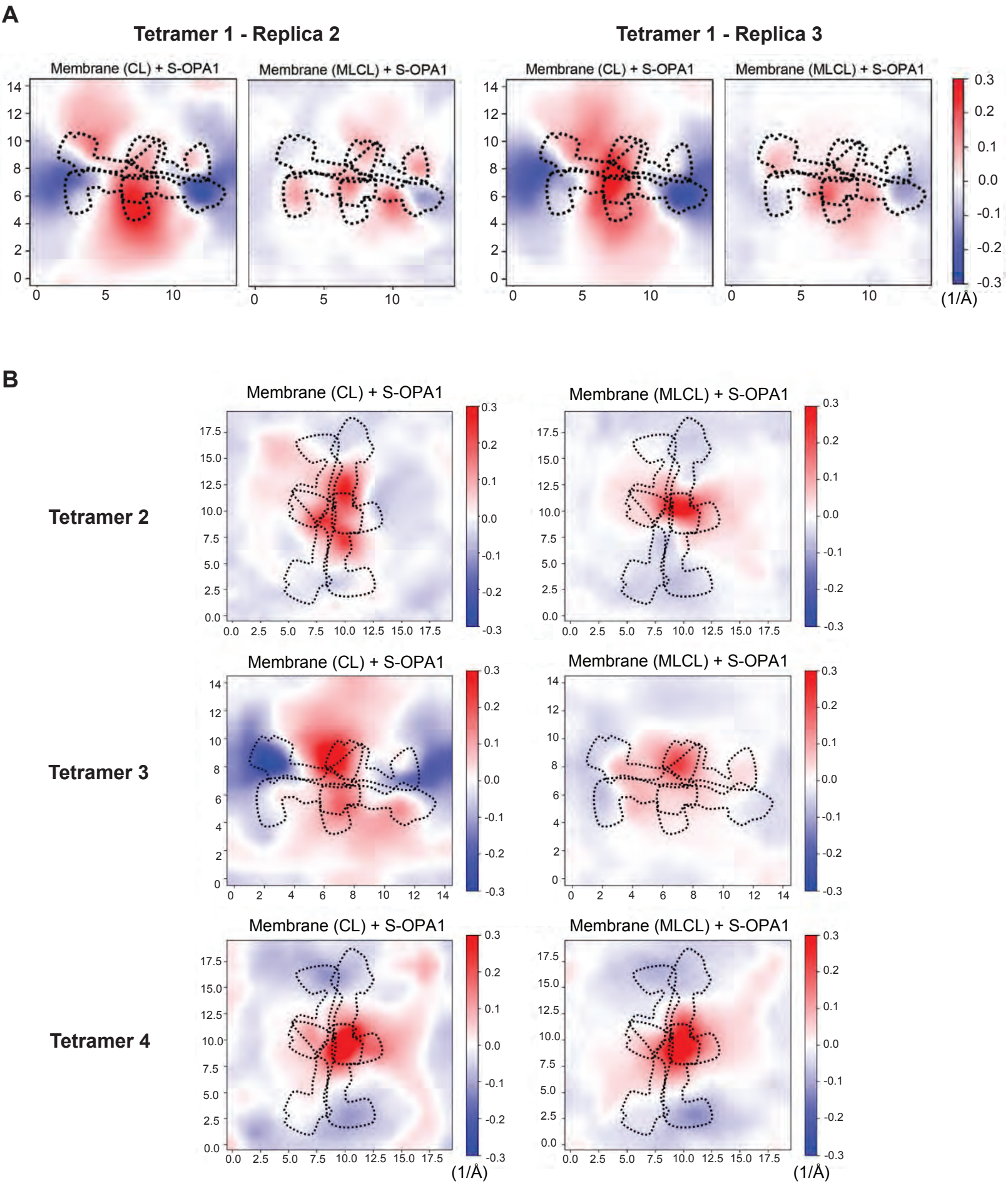

Figure S4

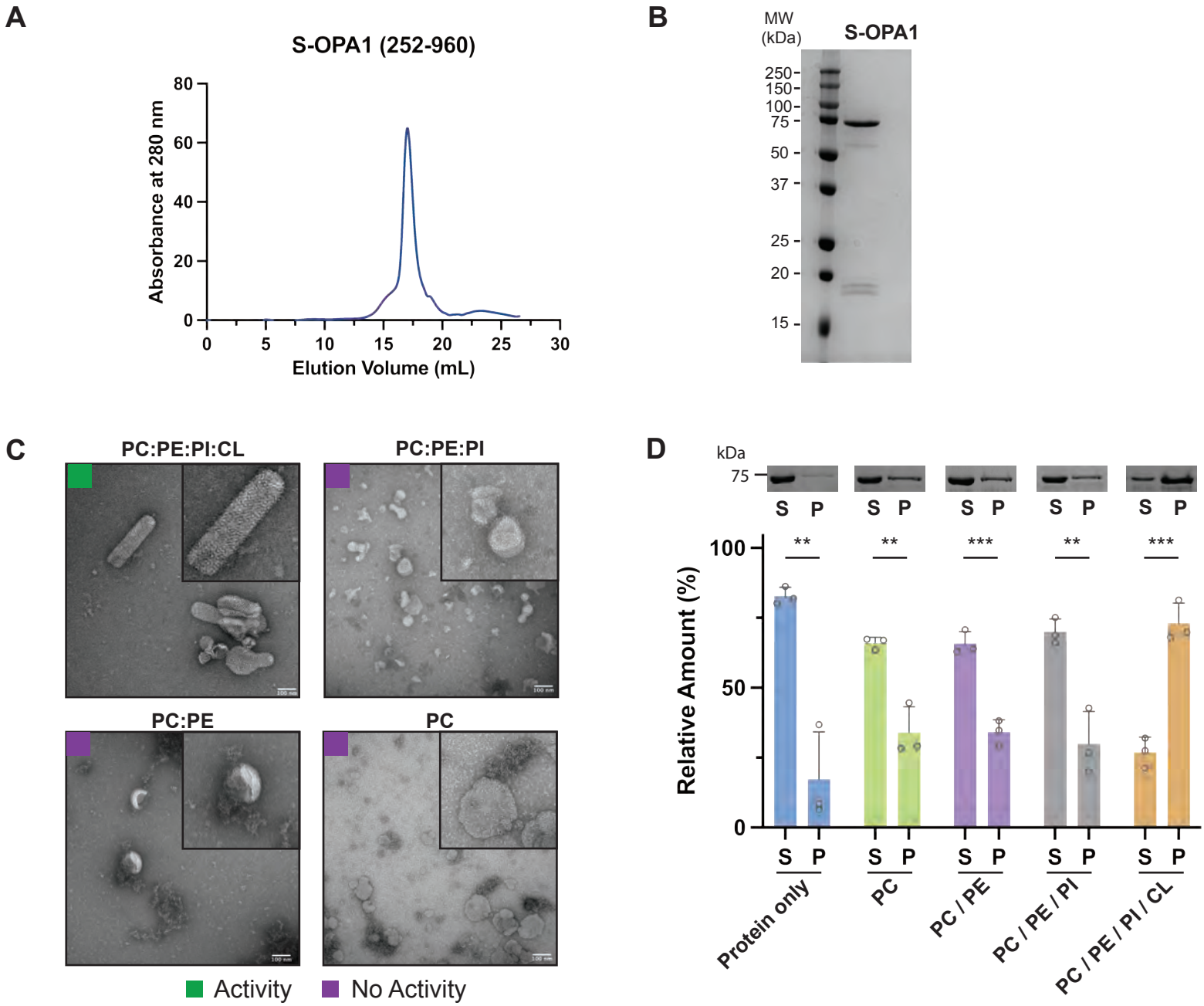

Figure S5

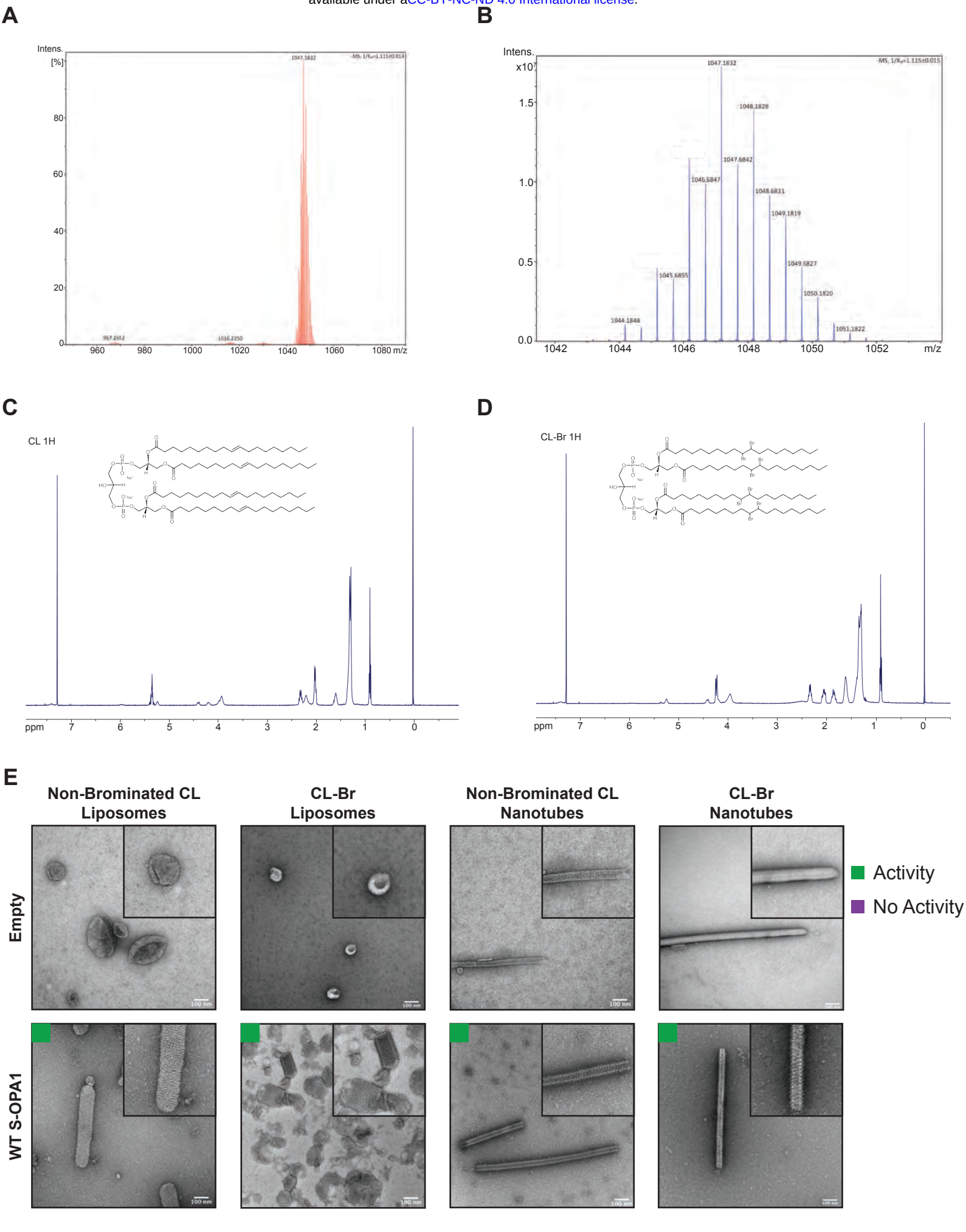

Figure S6

A

B

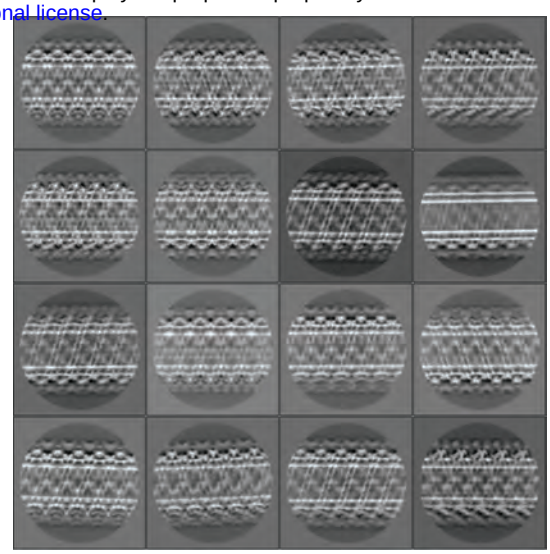

C

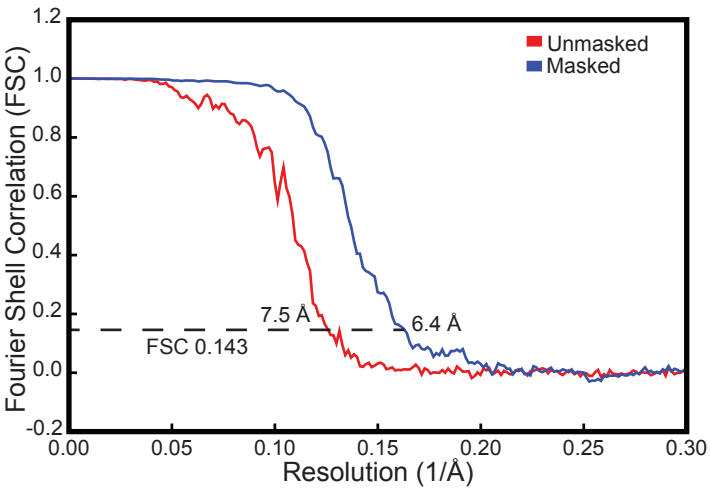

D

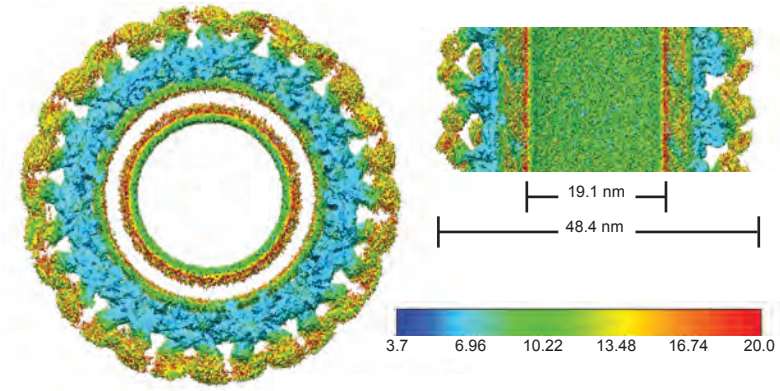

E

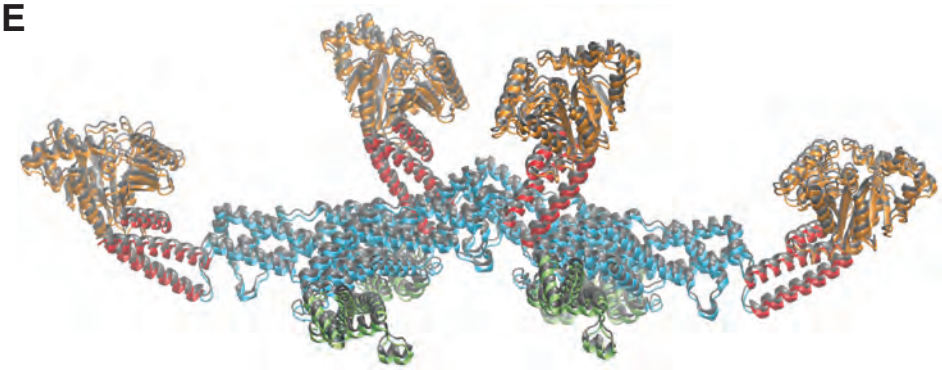

0.78Å RMSD

Figure S7

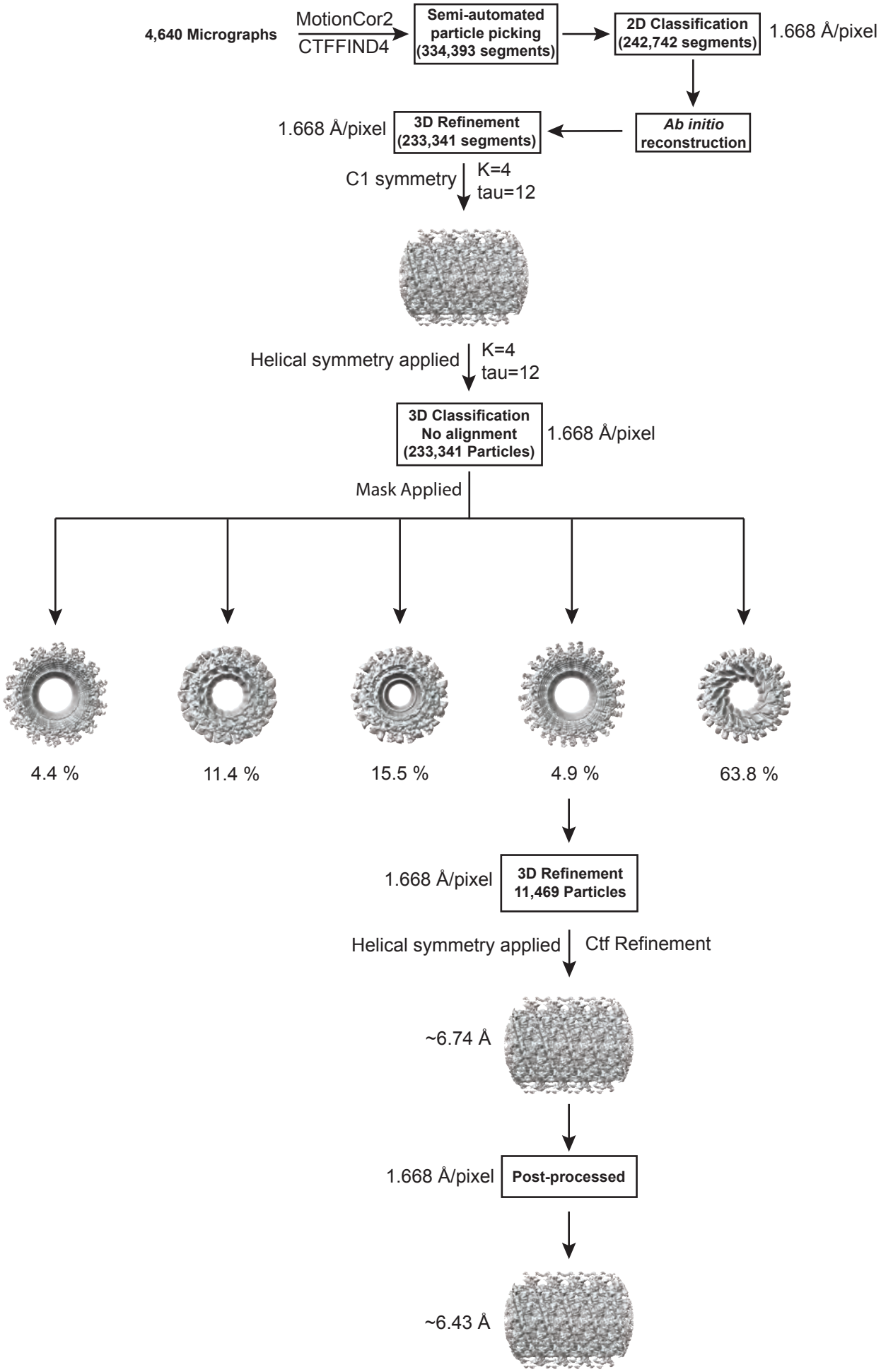

Figure S8

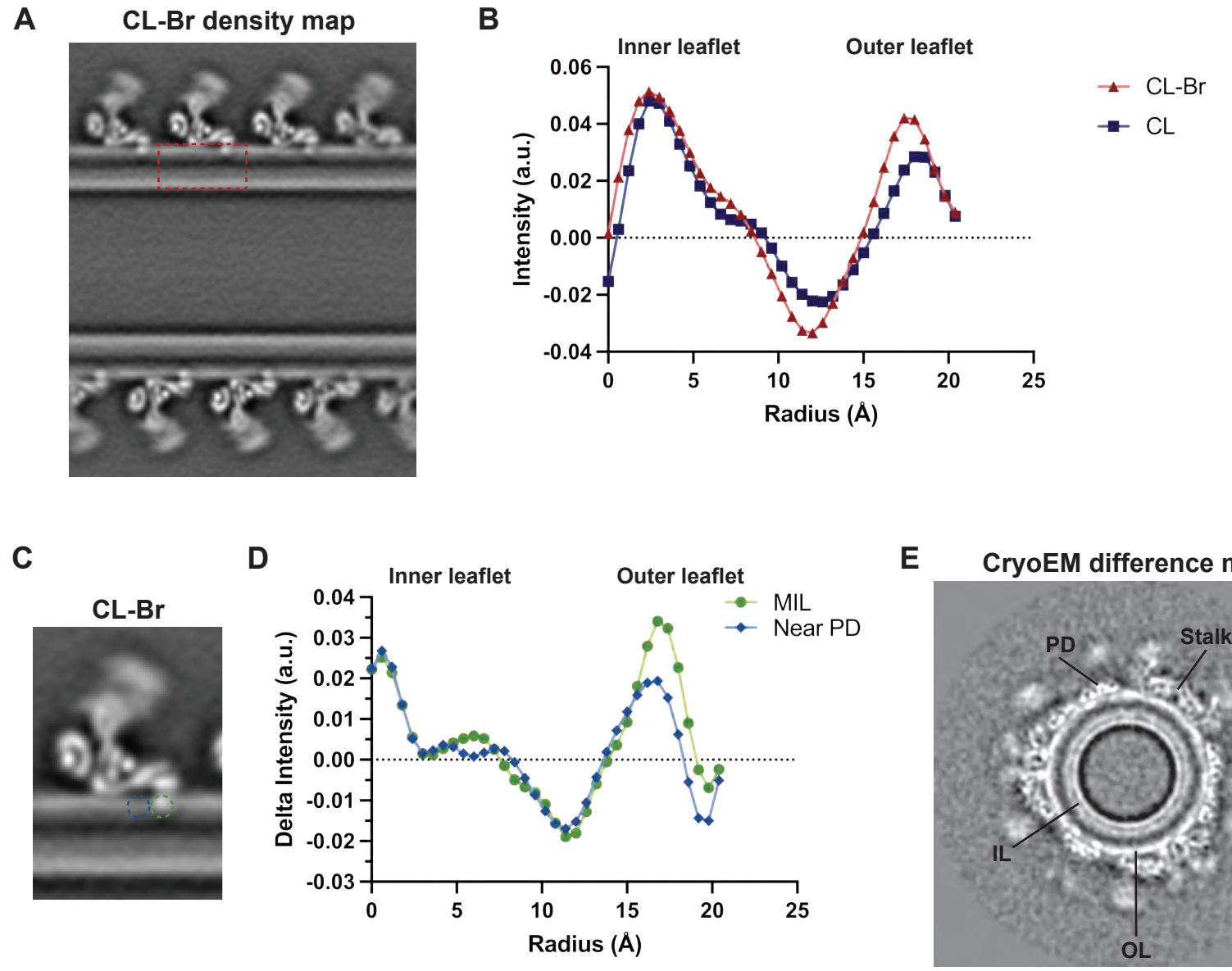

Figure S9

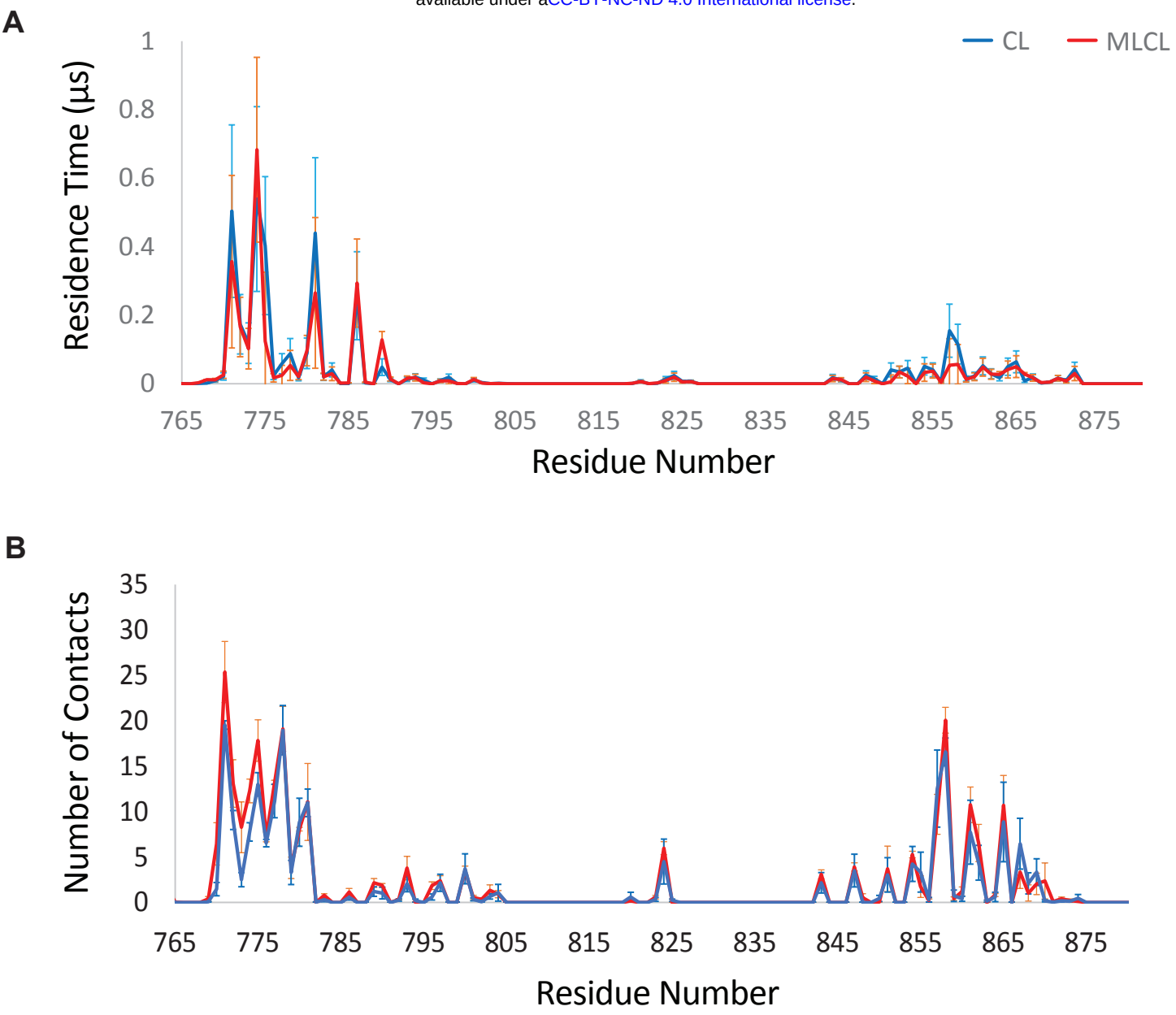

Figure S10

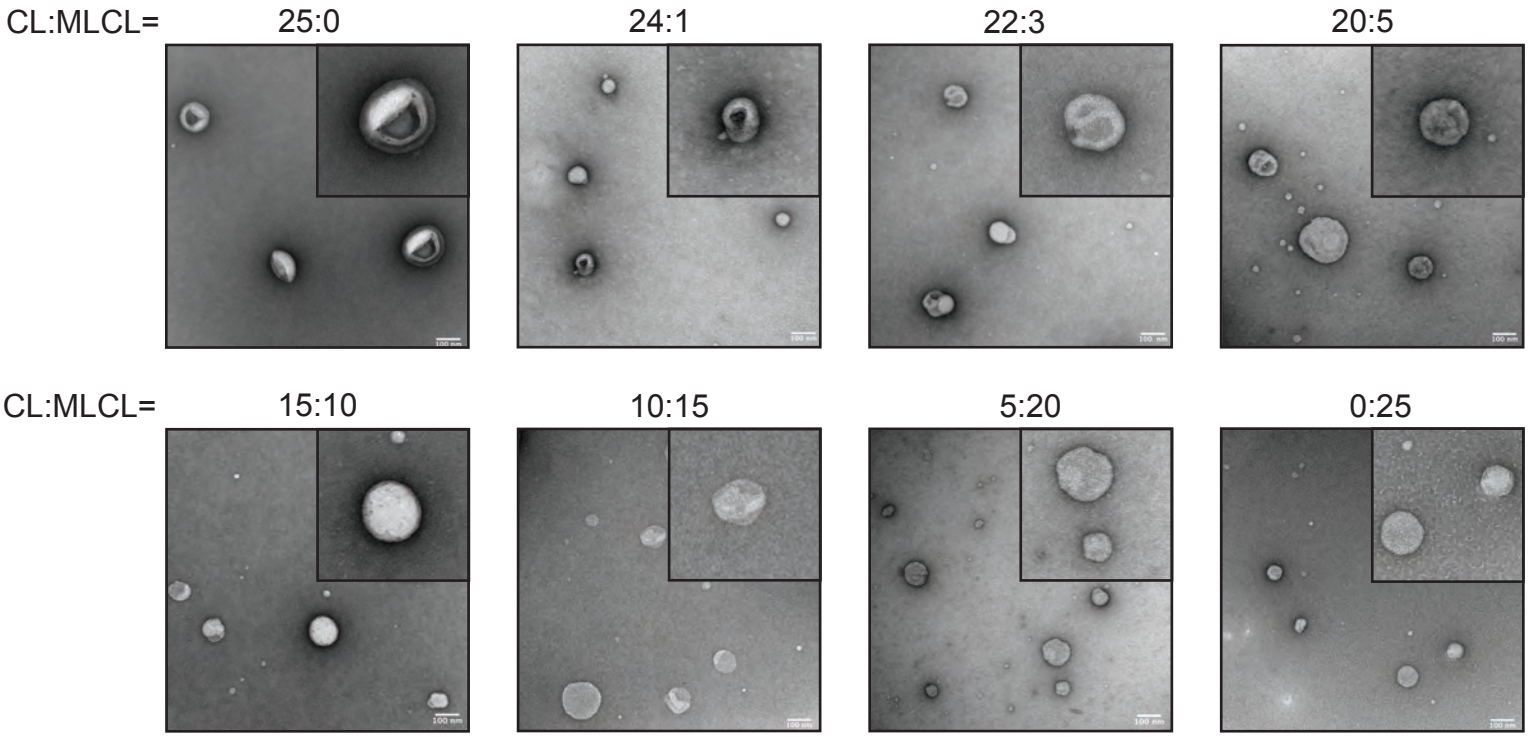

	Human S-OPA1 bound to CL-Br membranes (EMDB-43349)	
Data collection and processing		
Microscope	FEI Titan Krios	
Camera	Gatan K3 Summit	
Magnification	105,000x	
Voltage (kV)	300	
Electron exposure (e^-/ Å^2)	65	
Defocus (um)	0.5 to 1.5	
Pixel Size (Å)	0.834	
Symmetry imposed	Helical	
Micrographs (no.)	4,640	
Initial particle images (no.)	233,341	
Final particle images (no.)	11,469	
Map resolution (Å)	6.4	
FSC threshold	0.143	
Map resolution range (Å)	4.8 to 8.1	4.8 to 8.2
Models Generated (PDB code)	8VLZ	8VM4
Refinement		
Initial model used (PDB code)	8CT1	
Model resolution (Å)	6.4	
FSC threshold	0.143	0.143
Map sharpening B factor (Å^2)	-316.754	
Model composition		
Nonhydrogen atoms	22,723	
Protein residues	2,792	
B factors (Å^2) – min		
Protein	112.87	131.06
R.m.s deviations		
Bond lengths (Å)	0.002	0.002
Bond angles (°)	0.385	0.333
Validation		
MolProbity Score	1.16	1.19
Clashscore	3.68	4.06
Poor rotamers (%)	0.0	0.0
Ramachandran plot		
Favored (%)	99.57	99.57
Allowed (%)	0.43	0.43
Disallowed (%)	0.0	0.0

A

Liposome #	POPC (%)	POPE (%)	L-PI (%)	CL (%)
1	100	0	0	0
2	78	22	0	0
3	70	22	8	0
4	45	22	8	25

B

Liposome #	POPC (%)	POPE (%)	L-PI (%)	CL (%)	MLCL (%)
5	45	22	8	24	1
6	45	22	8	22	3
7	45	22	8	20	5
8	45	22	8	15	10
9	45	22	8	10	15
10	45	22	8	5	20
11	45	22	8	0	25

C

Liposome #	POPC (%)	POPE (%)	L-PI (%)	CL-Br (%)	GalCer (%)
12	45	22	8	25	0
13	0	0	0	10	90